Symmetries and optical transitions of hexagonal quantum dots in GaAs/AlGaAs nanowires

Guro K. Svendsen,* Johannes Skaar, and Helge Weman
Department of Electronics and Telecommunications, Norwegian University of Science and Technology, Trondheim, Norway

Marc-André Dupertuis
Laboratory of Physics of Nanostructures, Ecole Polytechnique Fédérale de Lausanne (EPFL), CH-1015 Lausanne, Switzerland
(Received 5 December 2014; published 10 November 2015)

We investigate the properties of electronic states and optical transitions in hexagonal GaAs quantum dots within $Al_{0.3}Ga_{0.7}As$ nanowires, grown in axial direction [111]. Such dots are particularly interesting due to their high degree of symmetry. A streamlined postsymmetrization technique based on class operators (PTCO) is developed which enables one to benefit from the insight brought by the maximal symmetrization and reduction of fields (MSRF) approach reported by Dalessi *et al.* [Phys. Rev. B **81**, 125106 (2010)], *after* having solved the Schrödinger equation. Definite advantages of the PTCO are that it does not require modification of existing code for the calculation of the electronic structure, and that it allows to numerically test for elevated symmetries. We show in the frame of a four-band $k \cdot p$ model that despite the fact that the D_{6h} symmetry of the nanostructure is broken at the microscopic level by the underlying zinc-blende crystal structure, the effect is quite small. Most of the particularities of the electronic states and their optical emission can be understood by symmetry elevation to D_{6h} and the presence of approximate azimuthal and radial quantum numbers.

DOI: 10.1103/PhysRevB.92.205303 PACS number(s): 61.50.Ah, 81.07.Gf, 78.67.Hc, 11.30.Qc

I. INTRODUCTION

Semiconductor nanowires have emerged as promising building blocks for realization of various nanoscale optoelectronic devices [1]. Nanowire technologies enable heterostructures with a high level of flexibility in terms of geometry and material composition [1]. In particular, growth of site controlled quantum dots (QDs) within nanowires shows significant advantages compared to more conventional self-assembled QDs (Stranski-Krastanov) [2,3], and bright single-photon emitters have been demonstrated in a range of materials using nanowire QDs [2–6].

QDs may be used in quantum information and cryptography technologies, e.g., for emission of entangled photon pairs. High symmetry is helpful to limit fine-structure splitting of excitonic states, and highly beneficial for polarization entanglement. In this respect, nanowire QDs are especially suitable as they may be highly symmetric, often with a hexagonal cross section. QDs within nanowires grown in the high-symmetry direction [111] are suggested as ideal sources for emission of entangled photon pairs [7–10]. Cascaded emission spectra, possibly enabling such pairs, have also been measured experimentally [6]. Generation of entangled photons is also possible in self-assembled QDs, in particular, InGaAs/GaAs QDs grown on [111] substrates are proposed to be ideal for such generation, due to the threefold axis of symmetry perpendicular to this surface [8]. Furthermore, QDs may enable quantum computation by using the electron spin as a quantum bit [11]. QDs grown in inverted pyramids on [111] GaAs substrates [10] have proven to be promising in this respect.

With increasing control of heterostructure shape and material composition, e.g., through nanowire growth, comes the possibility to fabricate structures according to optimized design. Theoretical models, e.g., providing insight into the nature of electronic states are essential in such optimization. In this work, we calculate the electronic states and optical transitions in hexagonal GaAs/AlGaAs nanowire QDs and analyze the results taking advantage of their high symmetry. A detailed procedure for full-depth symmetry analysis and reduction of computational domain has been presented previously by Dalessi *et al.* [12], and has been called maximal symmetrization and reduction of fields (MSRF). Here, we pursue this effort by developing a procedure alleviating recoding of computer programs: a postsymmetrization technique using class operators (PTCO). The PTCOis very general and applies independently of the method employed for the calculation of the electronic structure ($k \cdot p$, tight binding, etc.). It also provides a systematic and flexible procedure to test possible elevated symmetries.

In Sec. II, relevant theoretical studies of similar semiconductor heterostructures are considered, and we present the general features of the $k \cdot p$ model used in this paper. The explicit QD under consideration is described in Sec. III, and the symmetries are identified, providing the premises to optimally choose the basis for the $k \cdot p$ Hamiltonian. Having fully specified the numerical model, we describe the pertaining symmetry implications on the QD eigenstates in Sec. IV. The PTCOis then presented in Sec. V. Sections VI and VII contain the numerical calculations, analyzed using the PTCO. We show in Sec. VI that the analysis gives rise to a deeper understanding of all the electronic states, in particular of the level sequences. In Sec. VII, we investigate the fine structure of the spectrum of squared momentum matrix elements. We prove that symmetry elevation to D_{6h} and the existence of azimuthal and radial quantum numbers are necessary ingredients to explain many missing/weak optical transitions.

II. QUANTUM DOT DESCRIPTION AND $k \cdot p$ MODEL

Despite much activity in the experimental realization of nanowire QDs, there has until now been very little attention

*Currently at Norwegian Defence Research Establishment (FFI), NO-2027 Kjeller, Norway; guro.svendsen@gmail.com

towards numerical calculations of the electronic states. Niquet *et al.* [13] did perform calculations of strained InAs/InP nanowire QDs using a tight-binding model. The optical transitions were given and labeled using group symmetry. The QDs were, however, approximated as cylinders; cylindrically shaped QDs grown in the [111] direction of a wurtzite structure will inherit the limited C_{3v} symmetry of the crystal. Of related interest is also the work of Zhang *et al.* [14], considering excitons in nanowire QDs in the strained InGaN/GaN material system, using an effective mass approximation. Nanowires in the GaAs/AlGaAs material system considered in the current paper were treated by Kishore *et al.* [15] using the $k \cdot p$ model, but no calculations exist, to our knowledge, of nanowire QDs within this material system.

The $k \cdot p$ theory, originally intended for the calculation of band structures of crystalline solids, has been widely used for calculation of electronic states in heterostructures including QDs. Large emphasis has been on the strained self-assembled QDs [16–20], also including calculations on GaAs/AlGaAs QDs [20].

QDs with hexagonal shape were studied numerically using the $k \cdot p$ model in Ref. [16], but no explicit usage was made therein of the symmetry properties. On the opposite, Ref. [21] presents a strictly qualitative symmetry enumeration of electronic states and optical transitions in hexagonal QDs, without calculations.

Care should be taken to distinguish between the symmetry of any simplified numerical model and the physical system itself. The symmetry-preserving ability of the $k \cdot p$ model has been investigated numerically [22], demonstrating that the real symmetry of any structure can be accounted for upon inclusion of enough bands and interface terms.

We shall use a simple $k \cdot p$ model to describe the states of a GaAs QD within an AlGaAs nanowire, and demonstrate PTCO in a fairly simple framework. The conduction band electrons will be described with an effective mass model, and the valence band holes will be described with a four-band Luttinger Hamiltonian.

The conduction band involves electrons which can be described using a simple effective mass approximation, ignoring mixing with other bands [12]

$$H = -\frac{\hbar^2}{2m_0}\nabla\frac{1}{m^*(\mathbf{r})}\nabla + V_{\mathrm{CB}}(\mathbf{r}). \tag{2.1}$$

Here, ∇ is the three-dimensional (3D) differential operator $\nabla = \frac{\partial}{\partial x}\mathbf{u_x} + \frac{\partial}{\partial y}\mathbf{u_y} + \frac{\partial}{\partial z}\mathbf{u_z}$, $m^*(\mathbf{r})$ is the effective electron mass in units of the electron mass m_0, and $V_{\mathrm{CB}}(\mathbf{r})$ is the effective confinement potential for electrons in the conduction band. The envelope function ψ_n of energy level n is given by the Schrödinger equation

$$H\psi_n = E_n\,\psi_n. \tag{2.2}$$

The $j = \frac{1}{2}$ spinorial nature of conduction band states can be restored later; the exact procedure is given in Ref. [23].

Band mixing and spin cannot similarly be ignored for holes. The top six valence bands can be described as multiplet states with spin $j = \frac{3}{2}$ and $\frac{1}{2}$ [24]. When the energy separation to the latter multiplet (split-off band) is sufficient, the coupling can be ignored, and one is left with a four-valence-band $k \cdot p$ model. The 4×4 Luttinger Hamiltonian for diamond can then be used if one neglects inversion symmetry breaking, which is small in GaAs/AlGaAs. This leads to [24,25]

$$H = \frac{-\hbar^2}{m_0}\begin{pmatrix} p+q & -s & r & 0 \\ -s^+ & p-q & 0 & r \\ r^+ & 0 & p-q & s \\ 0 & r^+ & s^+ & p+q \end{pmatrix} + V_{\mathrm{VB}}(\mathbf{r}). \tag{2.3}$$

Here, p,q,r,s are quadratic forms of differential operators acting on envelope functions. Their exact expressions depend on the Bloch function basis which will be chosen later after considering heterostructure symmetry. The polynomial coefficients are given in terms of the Luttinger parameters $\gamma_i(\mathbf{r})$, $i = 1 \ldots 3$, and $V_{\mathrm{VB}}(\mathbf{r})$ is the confinement potential. Valence band eigenstates are denoted $\underline{\psi}_n$ (underline distinguishes spinors from scalar functions) and satisfy a spinorial Eq. (2.2) with (2.3).

III. MODEL STRUCTURE AND ITS SYMMETRY

The model structure under consideration is a QD grown as an axial insert of GaAs within an $Al_{0.3}Ga_{0.7}As$ nanowire. A radial shell of $Al_{0.3}Ga_{0.7}As$ is grown around the dot so that it is surrounded by $Al_{0.3}Ga_{0.7}As$ in all directions. The growth direction defining the nanowire axis is the crystal direction [111], and the cross section is hexagonal. A schematic is shown in Fig. 1. Similar QD structures have been grown previously by Kats *et al.* [4] who obtained mixed crystal phases containing both wurtzite and zinc blende. Guo *et al.* [26] obtained pure zinc-blende GaAs/AlGaAs axial heterostructures which we shall now assume.

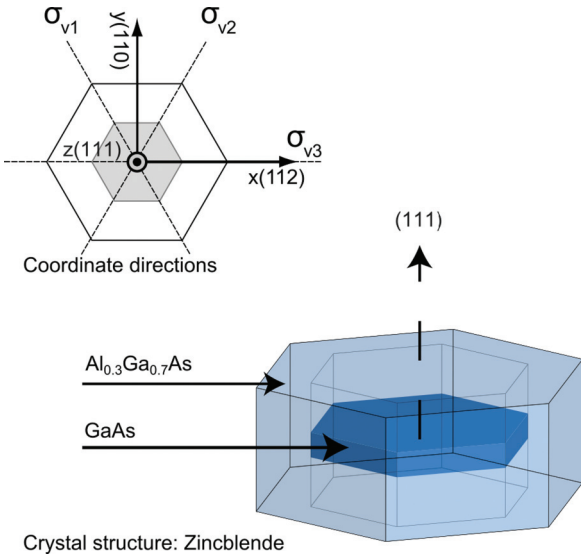

FIG. 1. (Color) Schematics of a hexagonal GaAs quantum dot within an $Al_{0.3}Ga_{0.7}As$ nanowire. Coordinate axes and crystal directions for the hexagonal QD are also shown. The main vertical symmetry planes $\sigma_{v1},\sigma_{v2},\sigma_{v3}$ are indicated.

The true QD symmetry is the common symmetry of the mesoscopic heterostructure (D_{6h}) and of the microscopic crystalline structure (C_{3v}). The conduction band Hamiltonian symmetry [Eq. (2.1)] is nevertheless the mesoscopic symmetry D_{6h}.

When the orientation of the crystal axes w.r.t the heterostructure is according to Fig. 1, the common symmetry elements are $\{e,C_3^+,C_3^-,\sigma_{v1},\sigma_{v2},\sigma_{v3}\}$ where C_3^+ and C_3^- are discrete $2\pi/3$ rotations and σ_{vi}, $i=1\ldots3$, are three vertical mirror operations. Hence, the valence band Hamiltonian [Eq. (2.3)] has C_{3v} symmetry.

The single group C_{3v} does describe operations performed on spatial coordinates only, and there are three irreducible representations (irreps) E, A_1, and A_2. The E irrep is a two-dimensional (2D) representation while the A_i irreps are one-dimensional (1D) [27]. On the other hand, double-group representations of C_{3v} must be used when half-integer spin is relevant like in the valence band. They comprise two 1D irreps ${}^1E_{3/2}$ and ${}^2E_{3/2}$ and a single 2D irrep $E_{1/2}$ [27].

Let $\mathcal{R}$ be a set of standard representation matrices corresponding to 3D space operations [12,28]. $\mathcal{R}(g)$ represents a change of coordinates indexed by group element g. Corresponding function space operators [27] are denoted $\vartheta(g)^{(3D)}$. With spin, such a change should be accompanied by a corresponding basis change in spin space, denoted $\vartheta(g)^{(j)}$ where g belongs to the double group. Composite spinorial operations are denoted by $\vartheta(g)=\vartheta(g)^{(3D)}\otimes\vartheta(g)^{(j)}$, where $\otimes$ is the tensor product. The set of 4×4 Wigner matrices $W(g)$ [28] characterize standard spin basis changes, also for the Luttinger Hamiltonian which is usually expressed in a Bloch function basis transforming like angular momentum, thus indexed by $|\frac{3}{2},m\rangle$ (m along a chosen quantization axis). Improper rotation matrices must be obtained using the corresponding matrix representative for spatial inversion.

To fully take advantage of the symmetry properties of the valence band Hamiltonian, a Bloch basis labeled by irreps of the double group is needed [12]:

$$\{|^2E_{3/2}\rangle,|E_{1/2},1\rangle,|E_{1/2},2\rangle,|^1E_{3/2}\rangle\}; \tag{3.1}$$

its elements are called heterostructure symmetrized Bloch functions (HSBF's), and correspond to suitable symmetrized superpositions of usual Bloch functions. For our C_{3v} Hamiltonian, the HSBF's are given by Eqs. (A11) and (A12) of Appendix section 2, whose ordering in Eq. (3.1) is important to preserve the form of the time-reversal symmetry operator [23].

Note that our choice of axes (Fig. 1) differs from that of Ref. [12], where the z quantization axis is chosen along the crystal direction $[\bar{1}10]$, i.e., correspond to the present y axis. Here, and in [23], the z axis is chosen along [111] which is also the nanostructure main axis, enabling a more direct correspondence between HSBF's weights and light/heavy hole (LH/HH) content along [111], which are most relevant (see following and in Secs. IV B and VI D 1).

In our HSBF basis, the p,q,r,s quadratic terms appearing in Eq. (2.3) are obtained using the bulk Luttinger Hamiltonian expressed in direction [111] (see, e.g., Ref. [25]), then changing its basis to the HSBF given in Ref. [23], and finally by replacing $k_j\to-i\frac{\partial}{\partial j}$ for $j=x,y,z$:

$$p=-\frac{1}{2}\left(\frac{\partial}{\partial x}\gamma_1\frac{\partial}{\partial x}+\frac{\partial}{\partial y}\gamma_1\frac{\partial}{\partial y}+\frac{\partial}{\partial z}\gamma_1\frac{\partial}{\partial z}\right), \tag{3.2a}$$

$$q=\frac{1}{2}\left(-\frac{\partial}{\partial x}\gamma_3\frac{\partial}{\partial x}-\frac{\partial}{\partial y}\gamma_3\frac{\partial}{\partial y}+2\frac{\partial}{\partial z}\gamma_3\frac{\partial}{\partial z}\right), \tag{3.2b}$$

$$r=-\frac{\partial}{\partial x}b\frac{\partial}{\partial x}+\frac{\partial}{\partial y}b\frac{\partial}{\partial y}-\frac{\partial}{\partial z}a\frac{\partial}{\partial x}-\frac{\partial}{\partial x}a\frac{\partial}{\partial z}, \tag{3.2c}$$

$$s=-\frac{\partial}{\partial y}a\frac{\partial}{\partial z}-\frac{\partial}{\partial z}a\frac{\partial}{\partial y}+\frac{\partial}{\partial x}b\frac{\partial}{\partial y}+\frac{\partial}{\partial y}b\frac{\partial}{\partial x}, \tag{3.2d}$$

where

$$a=\frac{\epsilon}{2}(-\gamma_3-i\sqrt{2}\gamma_2),\quad b=\frac{i\epsilon}{2}(\gamma_2+i\sqrt{2}\gamma_3) \tag{3.3}$$

with $\epsilon=\frac{1-i\sqrt{2}}{\sqrt{3}}$.

In the forthcoming analysis, it will be useful to distill the spinorial nature of the quantum states using the concept of light hole (LH) and heavy hole (HH) dominant character (because of band mixing the HH and LH states are mixed). Raw approximations for effective masses parallel and perpendicular to the [111] axis can be read from Eqs. (3.2a) and (3.2b) (assuming $r=s=0$), and are given by

$$m_\parallel^*=\frac{1}{\gamma_1\mp2\gamma_3}, \tag{3.4a}$$

$$m_\perp^*=\frac{1}{\gamma_1\pm\gamma_3}, \tag{3.4b}$$

where the upper and lower signs apply to HH and LH, respectively. For a normalized state $|\psi\rangle$, the weight of the LH contribution is defined by

$$w_{\mathrm{LH}}^{[111]}(\psi)\equiv|_z\langle3/2,1/2|\psi\rangle|^2+|_z\langle3/2,-1/2|\psi\rangle|^2, \tag{3.5}$$

and similarly for the HH, so $w_{\mathrm{LH}}^{[111]}+w_{\mathrm{HH}}^{[111]}=1$. Using the basis change between the HSBF basis and the $|\frac{3}{2},m\rangle$ basis quantized along [111], it is easy to show that

$$w_{\mathrm{LH}}^{[111]}(\psi)=|\langle E_{1/2},1|\psi|^2+|\langle E_{1/2},2|\psi\rangle|^2, \tag{3.6}$$

implying that the LH/HH character w.r.t. [111] is equivalent to the $E_{1/2}/^iE_{3/2}$ character in our C_{3v} HSBF, which is very convenient.

IV. SYMMETRY IMPLICATIONS ON NANOWIRE QUANTUM DOT STATES

A. Symmetry of envelope functions

We need to consider more in detail the transformation properties of spinors in order to exhibit envelope function properties peculiar to our nanowire QD. Under any double-group operation $g\in C_{3v}$, the spinor transformation reads as in the HSBF

$$\underline{\psi}'(\mathbf{r})=\vartheta_g[\underline{\psi}](\mathbf{r})=\underline{\underline{V}}^B(g)\underline{\psi}[\mathcal{R}(g)^{-1}\boldsymbol{r}], \tag{4.1}$$

where $V^B(g)$ are *block matrices* which are direct sums of representations ${}^2E_{3/2}\oplus E_{1/2}\oplus{}^1E_{3/2}$, and correspond to the HSBF-transformed Wigner matrices [12].

A seminal consequence of a symmetry group is that it is always possible [29] to find system eigenstates $\underline{\psi}$ by Γ,μ (Γ: irrep, μ: partner function index), such that the following characteristic transformation law holds:

$$\vartheta_g \underline{\psi}^{\Gamma}_{\mu}(\mathbf{r}) = \sum_{\nu=1}^{d_\Gamma} [D^{\Gamma}(g)]_{\mu,\nu} \underline{\psi}^{\Gamma}_{\nu}(\mathbf{r}), \tag{4.2}$$

where $D^{\Gamma}(g)$ is a set of representation matrices of dimension d^{Γ}. Suitable $D^{\Gamma}(g)$ are given in Ref. [12] (note the transposed multiplication table w.r.t. Ref. [27] since we use the passive point of view).

It is clear that Eqs. (4.1) and (4.2) strongly constrain the envelope function shapes. It was shown in [12] that they can be uniquely decomposed into *ultimately reduced envelope function* (UREF) components which themselves transform according to single-group irreps. This fact could be used to significantly reduce the computational domain. We will see here that it is also helpful in data postprocessing and analysis.

For our C_{3v} QD, the full valence band spinors corresponding to the various Γ,μ labels can be expressed in terms of UREFs in the following form:

$$\underline{\psi}^{\,{}^1E_{3/2}} = \begin{pmatrix} \phi^{A_2} \\ \phi^{E}_1 \\ \phi^{E}_2 \\ \phi^{A_1} \end{pmatrix}, \tag{4.3a}$$

$$\underline{\psi}^{\,{}^2E_{3/2}} = \begin{pmatrix} [\phi^{A_1}]^* \\ -[\phi^{E}_2]^* \\ [\phi^{E}_1]^* \\ -[\phi^{A_2}]^* \end{pmatrix}, \tag{4.3b}$$

$$\underline{\psi}^{E_{1/2}}_1 = \begin{pmatrix} -\phi^{E}_2 \\ \frac{1}{\sqrt{2}}[\phi^{A_1} + \Phi^{E}_1] \\ -\frac{1}{\sqrt{2}}[\phi^{A_2} + \Phi^{E}_2] \\ \varphi^{E}_1 \end{pmatrix}, \tag{4.3c}$$

$$\underline{\psi}^{E_{1/2}}_2 = \begin{pmatrix} \phi^{E}_1 \\ \frac{1}{\sqrt{2}}[\phi^{A_2} - \Phi^{E}_2] \\ \frac{1}{\sqrt{2}}[\phi^{A_1} - \Phi^{E}_1] \\ \varphi^{E}_2 \end{pmatrix}. \tag{4.3d}$$

Here, simplified labels have been used for the envelope functions: double-group labels (global spinor and HSBF labels) are implicit and can be uniquely restored. They explicitly identify distinct UREFs in all independent parts of Eq. (4.3) [12].

Time-reversal symmetry induces an additional unique antilinear mapping between Kramers degenerate QD eigenstates (no magnetic field), in analogy to the $k \to -k$ mapping in quantum wires [23]. Therefore, in C_{3v} Kramers pairs can be labeled either by the two partners of the self-conjugated 2D irrep ($E_{1/2}$) or by the pair of mutually conjugated 1D irreps ($^1E_{3/2}$, $^2E_{3/2}$), and corresponding spinors must satisfy $K\underline{\psi}^{\,{}^2E_{3/2}} = \underline{\psi}^{\,{}^1E_{3/2}}$ and $K\underline{\psi}^{E_{1/2}}_2 = \underline{\psi}^{E_{1/2}}_1$. Here, our careful choice of HSBFs [23] ensures a standard form of the time-reversal operator, for the valence band $K = FK_0$, where $F_{j,k} = \delta_{k,(5-j)}(-1)^j$, $1 \leqslant (j,k) \leqslant 4$, and K_0 denotes conjugation. Therefore, in this case the UREFs appearing in (4.3a) are equal to the corresponding UREFs in (4.3b), and restrictions can be formulated for the $E_{1/2}$ UREFs [(4.3c) and (4.3d)]

$$\begin{aligned} &\varphi^{E}_i = \left(\phi^{E}_i\right)^* \\ &\phi^{A_i} = (\phi^{A_i})^* \Rightarrow \phi^{A_i} \text{ is real} \\ &\Phi^{E}_i = -\left(\Phi^{E}_i\right)^*, \Rightarrow \Phi^{E}_i \text{ is imaginary} \end{aligned} \quad , \; i = 1,2 \tag{4.4}$$

which are specific to QDs (similar only to $k = 0$ states in quantum wires).

Without spin conduction band envelope functions bear C_{3v} or D_{6h} single-group labels. In both cases, eigenstates can be either nondegenerate or twice degenerate. Due to time reversal, degeneracy is doubled when adding spin.

Having established the precise symmetry of every spinorial component using UREFs, we now propose to quantify the respective contributions of each irrep, assuming that the full spinors are all normalized to unity, i.e., $\|\underline{\psi}_j\| = 1$.

The UREFs appearing in a given set $\underline{\psi}^{\Gamma}_{\mu}(\mathbf{r})$ transform into each other according to $D^{\Gamma}(g)$ [Eq. (4.2)] and must be written in general as $\psi^{\Gamma,\Gamma_a}_{\Gamma_b,\mu_a}$. Double-group Γ_b label identifies the relevant HSBF block of $V^B(g)$, and single group (Γ_a,μ_a) labels every UREF. There may be internal redundancies within the UREFs due to their own transformation properties. We may define the weight of a subset of symmetry Γ_a within the block Γ_b of the spinor $\underline{\psi}^{\Gamma}_{\mu}$ (assuming like here that Γ_b occurs only once in Γ) [30]:

$$w^{\Gamma_b,\Gamma_a}\left(\underline{\psi}^{\Gamma}_{\mu}\right) = \left\|\psi^{\Gamma,\Gamma_a}_{\Gamma_b}\right\|, \tag{4.5}$$

which is independent of μ. In addition, $\|\psi^{\Gamma,\Gamma_a}_{\Gamma_b}\| = \|\psi^{\Gamma,\Gamma_a}_{\Gamma_b,\mu_a}\|$ is independent of μ_a by symmetry [30] (generalized Wigner-Eckart theorem); therefore, partner function indices μ and μ_a are not relevant anymore. The chosen normalization ensures $\sum_{\Gamma_b,\Gamma_a} d_{\Gamma_a} w^{\Gamma_b,\Gamma_a} = 1$. d_{Γ_a} appears because every partner function contributes equal weight.

B. Decomposing states into simple products: Dominant HSBF as DPGPS

The global symmetry (Γ,μ) of any heterostructure eigenstate in a $k \cdot p$ model is always linked with an expansion in terms of products of Γ_a,μ_a UREFs with Γ_b,μ_b HSBFs, using Clebsch-Gordan coefficients. In addition, often (when band mixing is not too large) there is an identifiable dominant term so that the first factor describes well the main spatial probability distribution, and the second factor encodes the main symmetrized spin information. For example, an $^1E_{3/2}$ state (4.3a) with the dominant weight in the first (A_1) component corresponds to the product state $\Gamma^{\text{hole}} = A_1 \otimes {}^1E_{3/2}$. We have called the relevant HSBF discrete point group pseudospin (DPGPS) [31], a name which emphasizes the existence of composition rules similar to ordinary spin, but using Wigner-Eckart theorem for point groups. This concept has proven crucially useful to understand the state multiplicity of excitonic and biexcitonic complexes in C_{3v} QDs [31].

The identification of a dominant product in the valence band is not as straightforward as in the conduction band. However, there is an easy way to picture HSBF valence band mixing and to identify dominance by computing the weight (4.5) of every UREF appearing in Eq. (4.3) (using functional projection operators on single-group irreps [29]). We shall see that it reveals the true product nature (i.e., DPGPS) of most of the lower-lying eigenstates.

One last comment regarding the DPGPS and its relationship with the HH/LH concept: As explained in Sec. III, the HH weight equals the combined weight of the two $E^i_{3/2}$ spinor components in C_{3v}. The valence band state of the previous example (typically our QD ground state) may therefore be classified as HH-like. As shown in Appendix section 3, the two corresponding "spin states" are distinct conjugated DPGPS in C_{3v}, and the two partners of $E_{3/2,g}$ DPGPS in D_{6h}. Similarly, LH-like spin states will be associated to the partners of $E_{1/2}$ DPGPS in C_{3v} and to those of $E_{1/2,g}$ DPGPS in D_{6h}.

V. POSTSYMMETRIZATION

Postsymmetrization has earlier been demonstrated by Gallinet *et al.* using projection operators [30]. We will now present the PTCO, a systematic and streamlined postsymmetrization method. Its purpose is to disentangle and classify numerical eigenstates with individual symmetry labels. The main advantages of the PTCO are twofold: (1) it can be used in combination with preexisting calculation codes for the electronic structure, with little additional numerical/theoretical work, and (2) it will allow to test and qualify possible approximate elevated symmetries. We stress again that the PTCO can be applied in the frame of much more complex models than our simple four-band model.

Postsymmetrization will be carried out within a subspace $\mathcal{S}$ spanned by a relevant set of computed eigenstates $\{\underline{\psi}_j,\ j = 1 \ldots d_{\mathcal{S}}\}$ of the Hamiltonian. $\mathcal{S}$ will be called the *solution space*. For example, in Sec. VI we will retain the lower 20 hole eigenstates. The states $\underline{\psi}_j$ may not be as symmetric as they should be in principle (either due to numerical errors or to the use of a nonsymmetric underlying grid). Postsymmetrization will aim at finding the best symmetrized states belonging to $\mathcal{S}$, on the basis of an assumed symmetry, either ideal or approximate.

For any Hilbert space operator F there is a matrix representation $O(F)$ in $\mathcal{S}$, with elements

$$O(F)_{i,j} = \langle \underline{\psi}_i | F \underline{\psi}_j \rangle. \tag{5.1}$$

We shall use the same notation for F and its $O(F)$ since the relevant space is clear from context.

Numerical eigenstates do not exactly obey Eq. (4.2) in the general case. They can be mixed in two ways. First, mixing can be due to the uncontrolled choice of the solvers within every degenerate manifold. This effect can be strong. Although it is compatible with the original symmetry, a disentanglement is necessary to enable the use of individual Γ,μ labels linked with standard irreps $D^{\Gamma}(g)$. Second, eigenstates can be mixed due to numerical inaccuracies, in particular for nonsymmetric grids. Such mixing is always weak when good convergence is achieved, except if some energy levels are very close to each other. In such case, even states of different symmetries can be mixed. The goal of PTCO, which is a global postsymmetrization method, is to disentangle both kinds of mixing *simultaneously*.

A. Postsymmetrization using class operators (PTCO)

We propose here a global procedure in solution space which does not throw away any information like a standard sequential projection procedure. The information is gathered from all states in one step. The method is not cumbersome, it is flexible and easy to use. New optimally symmetrized eigenstates are automatically generated, with classified and predetermined transformation properties.

The PTCO procedure is based on the concept of commuting class operators [32] C_i, $i = 1, \ldots, n_C$, which are constructed by summing symmetry operators over a given group class:

$$C_i = \sum_{g \in \mathcal{C}_i} \vartheta(g), \tag{5.2}$$

where the classes $\mathcal{C}_i$ consist of all elements that are mutually conjugate, i.e., $\forall\ g_1, g_2 \in \mathcal{C}_i\ \exists\ g \in \mathcal{G}$ such that $g_2 = g(g_1)g^{-1}$. Class operators are closed under multiplication, commute with each other and with every group operation [32], and their number n_C equals the number of irreps. For example, there are three classes in C_{3v}: the trivial class $\mathcal{C}_e = \{e\}$, the class of mirror operations $\mathcal{C}_\sigma = \{\sigma_{vi},\ i = 1,2,3\}$, and the class of rotations $\mathcal{C}_3 = \{C_3^+, C_3^-\}$.

The sought symmetrized basis vectors $\underline{\psi}^{\Gamma}_{\mu} \in \mathcal{S}$ should be eigenfunctions of all class operators, with eigenvalues λ_i^{Γ}, i.e., $C_i \underline{\psi}^{\Gamma}_{\mu} = \lambda_i^{\Gamma} \underline{\psi}^{\Gamma}_{\mu}$. By construction, one has [32]

$$\lambda_i^{\Gamma} = \chi_i^{\Gamma} \frac{|\mathcal{C}_i|}{d^{\Gamma}}, \tag{5.3}$$

where χ_i^{Γ} is the class character and $|\mathcal{C}_i|$ is the cardinality of $\mathcal{C}_i$.

The power of the class operators has been extensively described in a different context by Chen [32]. He showed, in particular, that the set of class operators linked with a canonical subgroup chain can be used to form a complete set of commuting operators (CSCO) for the group space. However, *in solution space one must include the diagonal Hamiltonian to generate a CSCO* since there may be multiple subspaces with the same symmetry. To distinguish partner functions linked with 2D irreps of C_{3v}, D_{3h}, D_{6h}, we shall always use $C_s = \{e,\sigma_{v1}\}$ as a canonical subgroup and add $\vartheta(\sigma_{v1})$ to the CSCO such that

$$\text{CSCO} = \{H, C_3, C_\sigma, \vartheta(\sigma_{v1})\}. \tag{5.4}$$

The trivial class operator $\mathcal{C}_e$ has been omitted since it corresponds to the identity.

To diagonalize most simply the CSCO operators, it is most practical to combine them all into a single global CSCO operator C by forming

$$C = \alpha_H H + \alpha_3 C_3 + \alpha_\sigma C_\sigma + \alpha_s \vartheta(\sigma_{v1}), \tag{5.5}$$

where the coefficients α ensure that C has no degeneracy. We shall use the respective magnitude of the α factors to set symmetrization priorities by weighting more importantly

selected CSCO operators; systematic guidelines for a judicious choice will be given in Sec. VI C.

Let us now summarize the PTCOprocedure. A matrix representation of C is constructed from Eqs. (5.1) and (5.5) in the raw eigenvector basis $\{\underline{\psi}_j,\ j = 1 \ldots d_S\}$, where H is diagonal. The diagonalization $V^\dagger C V = \Lambda$ then yields *in one automated run* the matrix elements V_{jk} which can be interpreted as the seeked coefficients of the new symmetrized H "eigenvectors" $|\overline{\underline{\psi}}_k\rangle$ in the raw basis $|\underline{\psi}_j\rangle$. The quotes and the overbar stress that in fact they are not anymore numerically exact eigenvectors of H. Nevertheless, they are in a way more physical since part of the due symmetry, which was broken by the numerical implementation, has been restored by the procedure. The symmetry recognition step is defined by the identification $k \to (\Gamma,\mu,l)$ (l enumerates by order of increasing energy states with identical Γ,μ). This step is immediate using PTCO since a careful choice of the α coefficients guarantees for every (Γ,μ) *a specific range* of the corresponding eigenvalues $\overline{c}^{\Gamma}_{i,\mu,l}$ (see Sec. VI C), hence, $|\overline{\underline{\psi}}_k\rangle \to |\overline{\underline{\psi}}^{\Gamma}_{\mu,l}\rangle$. The full postsymmetrized symmetrized spinors can be easily constructed with

$$\overline{\underline{\psi}}^{\Gamma}_{\mu,l} = \sum_j \langle \underline{\psi}_j | \overline{\underline{\psi}}^{\Gamma}_{\mu,l} \rangle \underline{\psi}_j \,. \tag{5.6}$$

Furthermore, it is of high interest to compute with the same matrices the average values of each original CSCO operator [Eq. (5.4)]. First,

$$\overline{E}^{\Gamma}_{\mu,l} = \langle \overline{\underline{\psi}}^{\Gamma}_{\mu,l} | H \overline{\underline{\psi}}^{\Gamma}_{\mu,l} \rangle \tag{5.7}$$

are the new corrected energies. One notes the presence of the index μ, meaning that the PTCO cannot restore completely the degeneracies lifted by the original numerical implementation! Nevertheless, we still expect very closely packed eigenvalues for each $(\Gamma,\ \mu,\ l)$ subspace. Second, the average values of the C_{3v} class operators

$$\overline{\lambda}^{\Gamma}_{i,\mu,l} = \langle \overline{\underline{\psi}}^{\Gamma}_{\mu,l} | C_i \overline{\underline{\psi}}^{\Gamma}_{\mu,l} \rangle \tag{5.8}$$

should be closely packed around the ideal value λ^{Γ}_i [Eq. (5.3)], with again a slight μ dependence. Their interest is that *they allow to obtain directly the* Γ*-symmetry weights* $w^{\Gamma}(\underline{\psi}) = \sum_\mu w^{\Gamma}_\mu(\underline{\psi})$ via the following convenient character projection formula:

$$w^{\Gamma}(\underline{\psi}) = \frac{d^{\Gamma}}{|\mathcal{G}|} \left| \sum_i \left(\chi^{\Gamma}_i\right)^* \overline{\lambda}^{\Gamma}_{i,\mu,l} \right|. \tag{5.9}$$

$w^{\Gamma}(\underline{\psi})$ constitutes a figure of merit of the achieved state symmetrization for $\underline{\psi}$. Individual weights for each partner function could also be obtained, but in a more cumbersome way, using $\langle \overline{\underline{\psi}}^{\Gamma}_{\mu,l} | \vartheta(\sigma_{v1}) \overline{\underline{\psi}}^{\Gamma}_{\mu,l} \rangle$.

To conclude, the PTCO is a global, integrated, and automated procedure to carry out postsymmetrization which straightforwardly delivers in addition all quantities of interest (e.g., improved energies and symmetry weights).

B. A hierarchy of symmetries

PTCO will first be used to symmetrize w.r.t. C_{3v}, with the CSCO of the previous section. C_{3v} symmetry is the true symmetry of the structure, only broken by the nonsymmetric underlying grid, as well as numerical errors. From the physical point of view, higher *approximate* symmetries such as C_{6v}, D_{3h} and D_{6h} may also be relevant.

The C_{6v} symmetry group is constructed from C_{3v} by adding mirror operations w.r.t. three intermediate vertical symmetry planes (σ_{di}, $i = 1 \ldots 3$), and D_{3h} by inclusion of the mirror operation of the horizontal symmetry plane (σ_h). Combining C_{6v} and D_{3h} leads to the mesoscopic symmetry D_{6h}. Both for C_{6v} and D_{3h}, there are three double-group 2D irreps $E_{1/2}$, $E_{3/2}$, and $E_{5/2}$. Their identical subduction to C_{3v} yields $E_{3/2} \to {}^1E_{3/2} \oplus {}^2E_{3/2}$, $E_{5/2} \to E_{1/2}$, and $E_{1/2} \to E_{1/2}$. Subduction is also similar for D_{6h}, but all irreps are doubled with *gerade/ungerade* types. All corresponding D^{Γ} matrices are given in Appendix section 1.

The degree of validity of elevated symmetries can be investigated by diagonalizing the corresponding new CSCOs. New class operators must then simply be added to C: $\mathcal{C}_6 = \{C_6^+, C_6^-\}$ for C_{6v} or $\mathcal{S}_3 = \{S_3^+, S_3^-\}$ for D_{3h} [27], which distinguish $E_{1/2}$ and $E_{5/2}$ irreps in both cases. For D_{6h} it is enough to include both simultaneously.

One thus sees the versatility of the PTCO: Aside from restoring true symmetry by postsymmetrization, it offers the possibility to investigate in a simple way the existence of a hierarchy of symmetries as ever cruder, *but informative*, approximations to the problem at hand.

Figure 2 presents a schematic summary of tools and a coherent strategy for symmetry analysis.

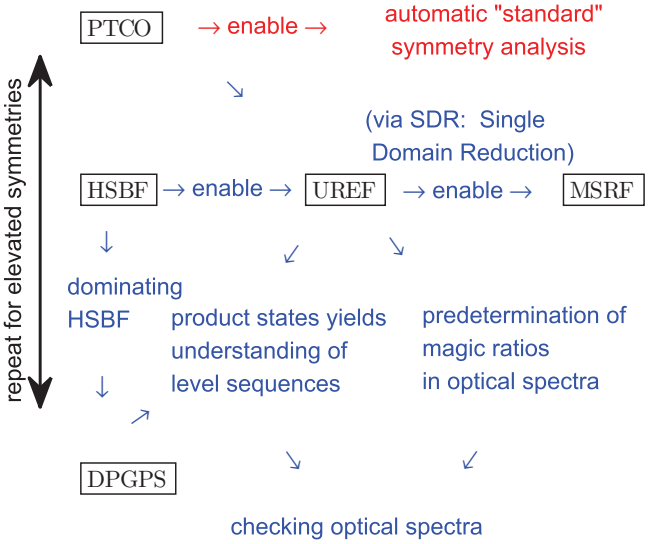

FIG. 2. (Color) Schematic summary of the tools and concepts of this paper, and their use for symmetry analysis (for acronyms, see main text). An initial first "guess" of the symmetry is a prerequisite. The process can be iterated easily for testing the presence of elevated symmetries.

TABLE I. Parameters for $k \cdot p$ simulation, at 0 K.

Effective mass [33]	GaAs: $m^* = 0.067$, AlAs: $m^* = 0.15$
Luttinger par.[a] [33]	GaAs: $\gamma_1 = 6.9800$, $\gamma_2 = 2.0600$, $\gamma_3 = 2.9300$ AlAs: $\gamma_1 = 3.7600$, $\gamma_2 = 0.8200$, $\gamma_3 = 1.4200$
Band gap [33]	$E_g^{\mathrm{GaAs}} = 1.519$ eV, $E_g^{\mathrm{AlAs}} = 3.099$ eV $E_g(x) = (1-x)E_g^{\mathrm{GaAs}} + xE_g^{\mathrm{AlAs}} - x(1-x)c$ $c = -0.127 + 1.310x$
Band offset ratio [34]	60.4 : 39.6
Band offsets	$E_v = 0.396\, E_g(x)$, $E_c = 0.604\, E_g(x)$

[a]Luttinger parameters for $Al_{0.3}Ga_{0.7}As$ are found using linear interpolation of VB effective masses and their anisotropy [33].

VI. NUMERICAL RESULTS

We consider a GaAs QD as described in Sec. II. The length of the hexagon edges is 20 nm, and the axial length of the dot is 5 nm. An $Al_{0.3}Ga_{0.7}As$ shell of thickness 10 nm surrounds the QD in the transverse direction, with infinite potential outside. In the axial direction, the dot is surrounded by a thick layer of $Al_{0.3}Ga_{0.7}As$, sufficient to ensure that all probability distributions go to zero. Effective masses, Luttinger parameters, and potential profile parameters (band gap and band offsets) as function of aluminium concentration are summarized in Table I.

A. Numerical implementation, energies, convergence, and accuracy

We used a finite difference approach on a square grid, using 91 equidistant points in every direction. Figure 3 displays the cross section of the CB and VB confinement potentials. The slightly wavy lateral sides evidence the deviation of the discretization with respect to C_{6v} symmetry, which will later be ideally averaged by PTCO.

We computed the 10 lowest conduction band levels (without spin) and the 14 upper valence band levels. Their energies (with respect to the top of the valence band) are reported in the first column of Tables II and III, respectively. Note that the highest valence band level included here deviates from the top of the valence band by 39 meV, the split-off band is located $\Delta_{\mathrm{so}} = 341$ meV away. The goal of this section is to build in a simple way the information displayed in all other columns of these tables.

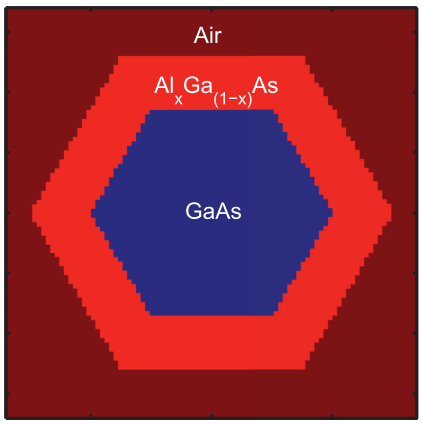

FIG. 3. (Color) Transverse cross section of the CB and VB potential.

Investigations of the numerical convergence indicate an energy accuracy of 1.7 meV for conduction band levels and 0.3 meV for the highest valence band level corresponding to similar spatial excitation. The lighter electron mass explains the lower accuracy for electrons despite equivalent numerical convergence. Note also that relative energy differences within each band are more accurate than the absolute values.

B. Conduction band eigenstates

Isosurfaces of the first few conduction band eigenfunctions $|\psi_{\mathrm{CB}}|^2$ are shown in Fig. 4. The full twice degenerate CB spinors $\underline{\psi_n}$ can easily be constructed [23]. In the present effective mass CB model one keeps the full D_{6h} heterostructure symmetry, therefore, every level in Fig. 4 is labeled by D_{6h} irreps, which bear g or u subscripts depending on whether they are even (*gerade*) or odd (*ungerade*) with respect to inversion. The possible single-group irreps of D_{6h} are [27] the 1D irreps $A_{1,g/u}$, $A_{2,g/u}$, $B_{1,g/u}$, $B_{2,g/u}$, and the 2D irreps $E_{1,g/u}$ and $E_{2,g/u}$, and their assignment to eigenfunctions of Fig. 4 using PTCO is explained in the following in more details for the VB. Table II summarizes the complete classification, also when including spin, and in C_{3v} symmetry.

TABLE II. Conduction band states and their final classification. The $(\Gamma,\mu)^{D_{6h}}$ labels are obtained taking the direct product of the UREFs and the DPGPS representations. The DPGPS for all conduction band states is $E_{1/2,u}$ (cf. Appendix section 2).

Level	E^{raw} (meV)	$(\Gamma,\mu)^{C_{3v}}$	UREF C_{3v}	$(\Gamma,\mu)^{D_{6h}}$	UREF D_{6h}	$\psi^{(\Gamma)^{D_{6h}}}_{(n_a,n_r)}$
1	1590	$E_{1/2}$	A_1	$E_{1/2,u}$	$A_{1,g}$	$\psi_{01}^{A_{1,g}}$
2,3[a]	1599, 1599	$E^j_{3/2}$, $E_{1/2}$	E	$E_{3/2,g}$, $E_{1/2,g}$	$E_{1,u}$	$\psi_{11}^{E_{1,u}}$
4,5[a]	1612, 1612	$E_{1/2}$, $E^j_{3/2}$	E	$E_{5/2,u}$, $E_{3/2,u}$	$E_{2,g}$	$\psi_{21}^{E_{2,g}}$
6	1617	$E_{1/2}$	A_1	$E_{1/2,u}$	$A_{1,g}$	$\psi_{02}^{A_{1,g}}$
7, 8	1626, 1630	$E_{1/2}$	A_1, A_2	$E_{5/2,g}$	$B_{1,u}$, $B_{2,u}$	$\psi_{31}^{B_{1,u}}$, $\psi_{31}^{B_{2,u}}$
9, 10[a]	1636, 1637	$E_{1/2}$, $E^j_{3/2}$	E	$E_{1/2,g}$, $E_{3/2,g}$	$E_{1,u}$	$\psi_{12}^{E_{1,u}}$

[a]Degenerate by symmetry. To enable better comparison with the valence band, we preserve individual level numbering.

TABLE III. Valence band states and their final classification.

Level	E^{raw} [a] (meV)	$\Delta E^{C_{3v}}$ [a] (μeV)	$\Delta E^{D_{6h}}$ (μeV)	$w_{\text{LH}}^{[111]}$ [b]	$(\Gamma,\mu)^{C_{3v}}$	UREF$^{C_{3v}}$ dominant	$(\Gamma,\mu)^{D_{6h}}$ dominant	UREF$^{D_{6h}}$ dominant	$\psi_{(n_a,n_r)}^{(\Gamma)^{D_{6h}}}$
1	−14.6	1.3	1.4	0.01	$E_{3/2}^{j}$	A_1	$E_{3/2,g}$	$A_{1,g}$	$\psi_{01}^{A_{1,g}}$
2,3	−20.4, −20.9	0.4, 0.5	118.2, −111.5	0.04, 0.03	$E_{1/2}$	E	$E_{5/2,u}$, $E_{1/2,u}$	$E_{1,u}$	$\psi_{11}^{E_{1,u}}$
4, 5	26.4, 28.0	4.8, 14.9	541.9, −487.5	0.12, 0.08	$E_{1/2}$	E	$E_{5/2,g}$, $E_{1/2,g}$	$E_{2,g}$	$\psi_{21}^{E_{2,g}}$
6	−28.5	−16.5	−15.9	0.15	$E_{3/2}^{j}$	A_1	$E_{3/2,g}$	$A_{1,g}$	$\psi_{02}^{A_{1,g}}$
7, 10	−31.4, −35.0	6.3, −9.5	8.9, −12.1	0.25, 0.21	$E_{3/2}^{j}$	A_1, A_2	$E_{3/2,u}$	$B_{1,u}$, $B_{2,u}$	$\psi_{31}^{B_{1,u}}$, $\psi_{31}^{B_{2,u}}$
8, 9	−33.9, −34.6	−2.8, 8.5	319.8, −296.3	0.32	$E_{1/2}$	E	[c]$E_{1/2,u}$, $E_{5/2,u}$	$E_{1,u}$	$\psi_{12}^{E_{1,u}}$
11	−35.4	1.2	285.0	0.37	$E_{1/2}$	E	[c]$E_{1/2,g}$	$E_{2,g}$	$\psi_{41}^{E_{2,g}}$
12, 15	−37.8, −39.4	7.5, −29.5	−57.7, −281.8	0.42, 0.43	$E_{1/2}$	E	[c]$E_{1/2,g}$, $E_{5/2,g}$	$E_{2,g}$	$\psi_{22}^{E_{2,g}}$
13	−38.6	−3.5	−27.1	0.46	$E_{1/2}$	E	[c]$E_{5/2,u}$	$E_{1,u}$	$\psi_{51}^{E_{1,u}}$
14	−39.0	16.3	15.7	0.44	$E_{3/2}^{j}$	A_1	$E_{3/2,g}$	$A_{1,g}$	$\psi_{03}^{A_{1,g}}$

[a]Averaged over Kramers doublets.
[b]For the C_{3v} symmetrized basis.
[c]Intermixed symmetries.

C. Valence band eigenstates

The symmetry of valence band states is a much more complex matter, and we will utilize extensively PTCO. First, one wishes to symmetrize w.r.t. the true original C_{3v} symmetry, as the lack of symmetry of the underlying grid may strongly influence the choice of eigenstates within degenerate subspaces. PTCOwill also give quantitative information about the effect of the symmetrization process.

1. *Analysis of true C_{3v} symmetry*

The global CSCO operator C, used for postsymmetrization, is given for C_{3v} by Eq. (5.5), hence its eigenvalues are by

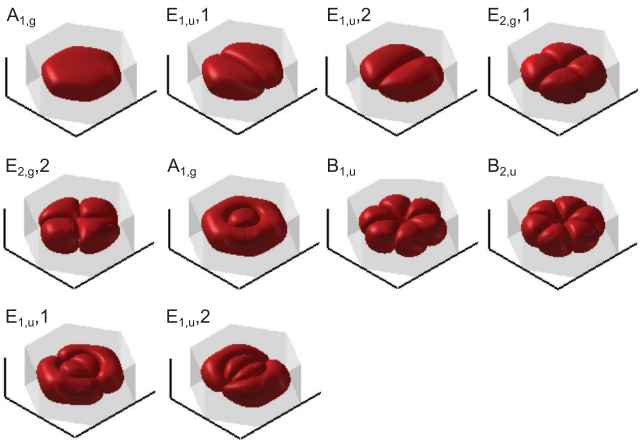

FIG. 4. (Color) Isosurfaces of conduction band eigenfunctions $|\psi_{\text{CB}}|^2$, for increasing energy levels, labeled by D_{6h} irreps (single group).

definition

$$c_{\mu,l}^{\Gamma} = \alpha_H \overline{E}_{\mu,l}^{\Gamma} + \sum_{i=3,\sigma,s} \alpha_i \overline{\lambda}_{i,\mu,l}^{\Gamma}, \tag{6.1}$$

where $\overline{E}_{\mu,l}^{\Gamma}$ and $\overline{\lambda}_{i,\mu,l}^{\Gamma}$ are given by Eqs. (5.7) and (5.8). It is worth noting that the $c_{\mu,l}^{\Gamma}$ eigenvalues can be tuned *a priori* using the α coefficients since we approximately know the corrected energies $\overline{E}_{\mu,l}^{\Gamma}$ (close to the raw values), as well as the ideal eigenvalues λ_i^{Γ} [Eq. (5.3)].

We now outline how to choose the α's to ensure not only well-separated eigenvalues $c_{\mu,l}^{\Gamma}$, but also to set *symmetrization priorities* by weighting more importantly relevant CSCO operators. Let us write the approximate spectrum of C [cf. Eq. (6.1)]

$$\tilde{c}_{\mu,l}^{\Gamma} = \alpha_H \overline{E}_{\mu,l}^{\Gamma} + \sum_{i=3,\sigma} \alpha_i \lambda_i^{\Gamma} + \alpha_s \lambda_{s,\mu}. \tag{6.2}$$

The last parameter α_s, which is related to the class operator of the subgroup $\mathcal{C}_s$, distinguishing different partner function indices μ, is now singled out to avoid confusion between the eigenvalues λ_i^{Γ} of C_{3v} and $\lambda_{s,\mu}$ of $\mathcal{C}_s$.

First, it is convenient to shift and normalize C by setting $\alpha_H = 1/\max_{\Gamma,\mu,l}(\overline{E}_{\mu,l}^{\Gamma} - E_0)$ where E_0 is the ground-state energy. The set of eigenvalues

$$c_{\mu,l}^{\Gamma} = \frac{\overline{E}_{\mu,l}^{\Gamma} - E_0}{\max\limits_{\Gamma,\mu,l} \overline{E}_{\mu,l}^{\Gamma} - E_0} + \tau_{\mu}^{\Gamma} \tag{6.3}$$

is then such that *the Hamiltonian range is unity*, and the symmetry-dependent remainder reads as

$$\tau_{\mu}^{\Gamma} = \alpha_s \lambda_{s,\mu} + \sum_{i=3,\sigma} \alpha_i \lambda_i^{\Gamma}. \tag{6.4}$$

TABLE IV. Equidistant parameters τ_μ^Γ chosen to separate between C_{3v} irreps and partner functions.

$\tau^{^2E_{3/2}}$	$\tau^{^1E_{3/2}}$	$\tau^{E_{1/2,1}}$	$\tau^{E_{1/2,2}}$
−3.5	−1.5	0.5	2.5

Second, the idea is to use the remaining α's to induce significant eigenvalue splittings between different symmetry labels via Eq. (6.4), facilitating eigenvector symmetrization and identification.

With the help of Eq. (5.3) we could predetermine well-separated τ_μ^Γ values, equidistant for C_{3v} symmetrization (see Table IV). The relative separation $\Delta\tau$ then specifies in a way a magnitude of symmetry splittings with respect to the normalized Hamiltonian spectrum, and thus corresponds to enforced priorities during rediagonalization. Choosing $\Delta\tau \gg 1$ would emphasize symmetry at the price of eventually remixing completely the Hamiltonian eigenstates. On the opposite, $\Delta\tau \ll 1$ would give small weight to symmetry considerations. Our empirical choice $\Delta\tau = 2$ is balancing both aspects and separates nicely different irreps for easy identification. It was found appropriate to improve the C_{3v} symmetry perturbed by the nonsymmetric underlying grid, in particular to optimally symmetrize degenerate states.

Having determined the α coefficients, we diagonalized the C operator in the solution space defined by the lowest 30 raw valence band states (including Kramers degeneracy). The remixing due to symmetrization is visualized in Fig. 5, where we display the norm of the matrix elements of the unitary symmetrization V. Figure 6 demonstrates that the energy changes ΔE for each level after symmetrization is very modest, confirming the quality of the raw results.

At large, we see clearly that symmetrization remixes essentially within degenerate Kramers doublets. There are no intertwined blocks, a situation that PTCO would nevertheless

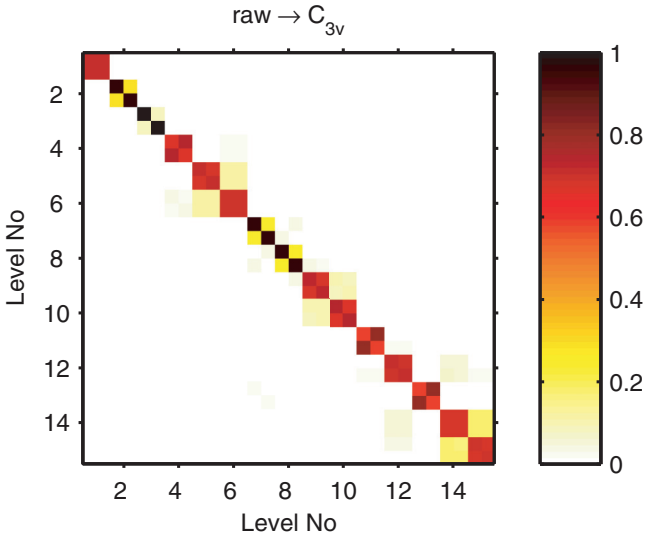

FIG. 5. (Color) Norms of the elements of the unitary symmetrization matrix V w.r.t. C_{3v}.

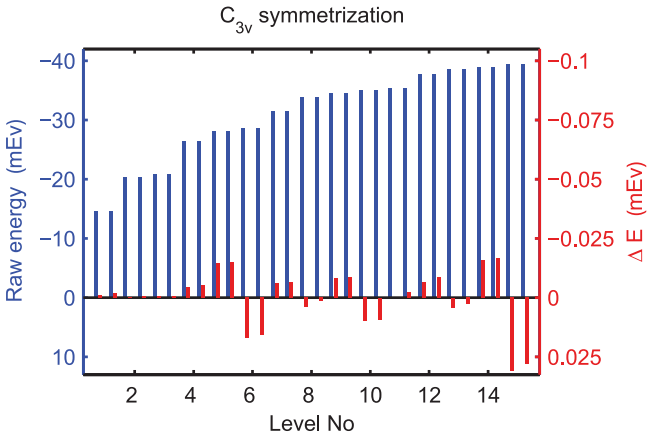

FIG. 6. (Color) Energy changes after C_{3v} symmetrization. Raw energy spectrum is shown in blue, and the difference between symmetrized and raw spectrum is shown in red (bright grey).

handle automatically, sorting and symmetrizing the respective sets of partner functions.

Figure 5 also evidences slight spurious off-diagonal mixing between different Kramers doublets (e.g., levels 5-6), which is amplified by energy proximity, as clearly displayed by Fig. 6. It is also associated with doublets *of different symmetry* (cf. Fig. 7), which is a signature of symmetry breaking by the underlying grid. A systematic behavior is observed for all mixed pairs of such doublets (levels 5-6, 9-10, and 14-15), and consistently correspond to the biggest energy changes (albeit very small <0.05%). Such effects would be very cumbersome to correct using a standard stepwise projection operator procedure.

The level of achieved C_{3v} symmetrization is analyzed for all 30 computed states in Fig. 7 using the symmetry weights $w_\mu^\Gamma(\overline{\psi}_\mu^\Gamma)$ for double-group irreps. The eigenstates are very pure and well grouped in conjugated doublets, which confirms as much the symmetry of the QD as the excellent convergence, or the PTCO procedure.

We proceed to the next levels of the C_{3v} symmetry analysis, considering UREFs and associated single-group irreps. In

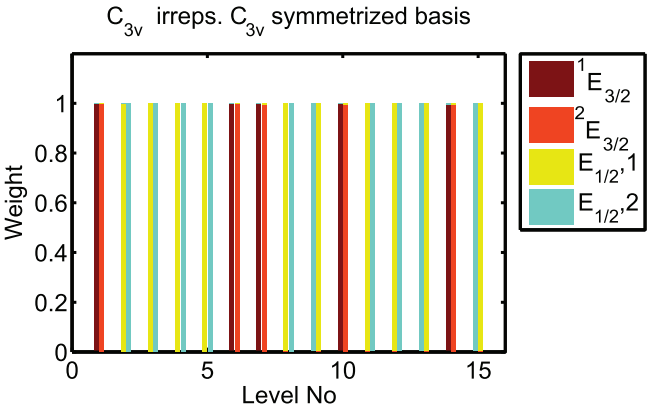

FIG. 7. (Color) Double-group weights $w_\mu^\Gamma(\overline{\psi}_\mu^\Gamma)$ w.r.t. the C_{3v} irreps after C_{3v} symmetrization.

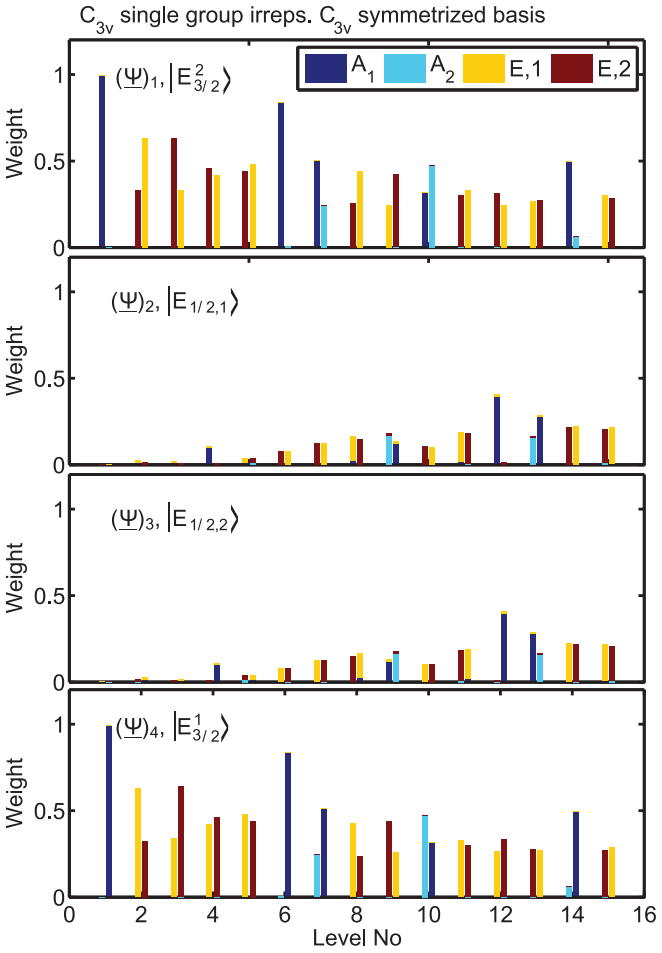

FIG. 8. (Color) Single-group weight $w_\alpha^{\Gamma_a}(\psi_{\mu,\beta}^{\Gamma,\Gamma_b})$ for each level after C_{3v} symmetrization.

Fig. 8, the (Γ_a,α) weights

$$w_\alpha^{\Gamma_a}\left(\psi_{\mu,\beta}^{\Gamma,\Gamma_b}\right) = \left|C_{\mu,\beta;\alpha}^{\Gamma,\Gamma_b^*;\Gamma_a}\right| w^{\Gamma_b,\Gamma_a}\left(\underline{\psi}_\mu^\Gamma\right) \tag{6.5}$$

are plotted for each HSBF envelope function $\psi_i \equiv \psi_{\mu,\beta}^{\Gamma,\Gamma_b}$. Note that they differ from $w^{\Gamma_b,\Gamma_a}(\psi^\Gamma)$ [Eq. (4.5)] by a Clebsch-Gordan coefficient, which in C_{3v} differs from unity only in the central component of the $E_{1/2}$ spinor.

In Fig. 8, we first note that the UREF irreps are in accordance with Eq. (4.3). However, there is a striking unbalance between weights of the partner functions in the $|^i E_{3/2}\rangle$ components of the $E_{1/2}$ states, most notably for levels 2 and 3 and 8 and 9. Due to time-reversal symmetry, the two $|^1 E_{3/2}\rangle$ HSBF components (or the two $|^2 E_{3/2}\rangle$ components) are mutual E-partner functions with the *same weights* on principle. We assume such unbalance can only occur from imperfect grid and mixing of nearby quasidegenerate levels with same symmetry, so that mixing cannot be well discriminated by C_{3v} symmetrization. This explanation is supported by the fact that each of the two concerned $E_{1/2}$ level pairs (2-3 and 4-5) has simultaneously opposite weight imbalance and closeby energies (Fig. 6). Actually, the presence of additional quasidegeneracies do alert us of the possible existence of approximate elevated symmetries, which may be able to correctly remix the relevant states.

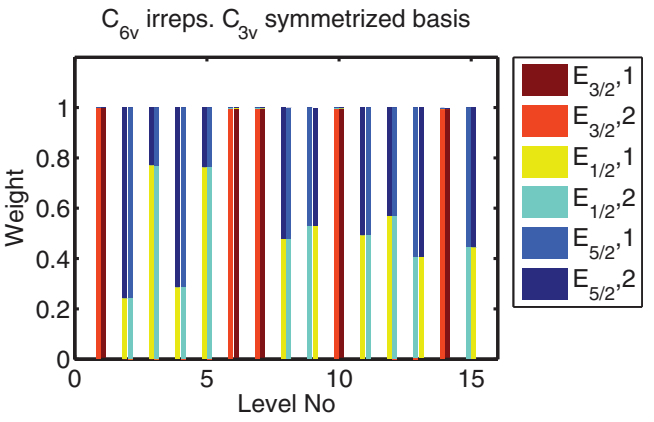

FIG. 9. (Color) Double-group weights of C_{3v}-symmetrized eigenstates w.r.t. the irreps of the elevated C_{6v} group.

2. *Analysis of elevated C_{6v} and D_{3h} symmetries*

The quasidegeneracy of the first two $E_{1/2}$ levels hinted at the possible occurrence of approximate elevated symmetries. Such symmetries have previously been found both in theoretical [23] and experimental [9,31] work on [111] oriented C_{3v} heterostructures. Because the mesoscopic structure has D_{6h} symmetry, we shall now test for the possible existence of C_{6v}, D_{3h}, and D_{6h} elevated symmetries to see if there is a hierarchy and, if so, how it is organized.

Figure 9 displays the weights of the C_{3v}-symmetrized states according to C_{6v} double-group irreps (D_{3h}, not shown, was very similar). We see no change for $^i E_{3/2}$ states which are also well defined using C_{6v} or D_{3h}, in agreement with their subduction tables [27], which yield $E_{3/2} \to E_{3/2}^1 \oplus E_{3/2}^2$. For the remaining irreps, C_{6v} or D_{3h} subduction tables yields $E_{5/2} \to E_{1/2}$ and $E_{1/2} \to E_{1/2}$, in accordance with Figs. 7 and 9. However, we see clearly some irrep mixing which sometimes prevents unique labeling of these states in view of the elevated symmetry groups C_{6v} and D_{3h}, and demonstrates their approximate nature.

For closer investigation, we shall perform a further C_{6v} symmetrization, as proposed in Sec. V. This can be easily done by adding to the CSCO the class operator $\mathcal{C}_6$ (or $\mathcal{S}_3$ for D_{3h}) which allows to distinguish between the $E_{1/2}$ and $E_{5/2}$ irreps of the elevated group. Of course, one cannot expect the result to be more exact since they are not true symmetries of the QD, but perhaps the result will help determine what is the closest approximation. The τ symmetrization parameters for C_{6v} are given in Table V, and were again chosen to separate clearly the different irreps, but they are not anymore equidistant. The

TABLE V. Parameters τ_μ^Γ for symmetrization w.r.t. elevated symmetry groups C_{6v} and D_{3h}.

$\tau_1^{E_{3/2}}$	$\tau_2^{E_{3/2}}$	$\tau_1^{E_{1/2}}$	$\tau_2^{E_{1/2}}$	$\tau_1^{E_{5/2}}$	$\tau_2^{E_{5/2}}$
−3.5	−1.5	0.65	2.65	0.35	2.35

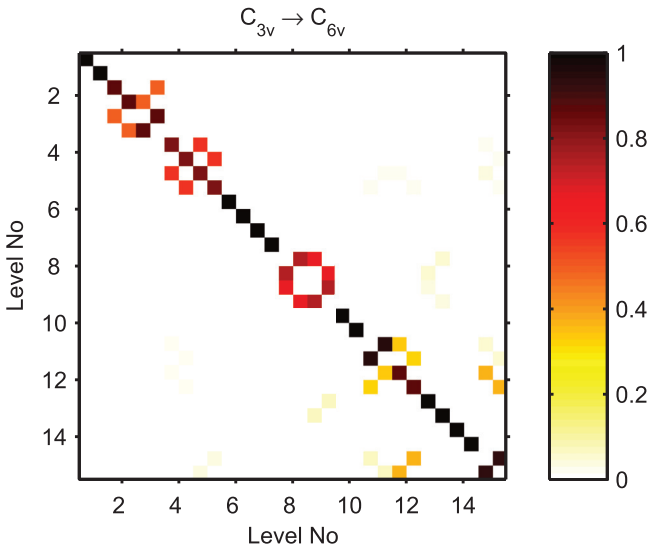

FIG. 10. (Color) Norms of the V_2 matrix elements, connecting the C_{6v}-symmetrized states to C_{3v}-symmetrized basis.

separation for irreps that are indistinguishable in C_{3v} has been chosen smaller than 1, keeping some Hamiltonian priority over the approximate symmetry.

With some surprise we found that D_{3h} symmetrization leads to nearly identical results w.r.t. C_{6v} symmetrization, both qualitatively and quantitatively, so the results are left out. It led to the classification in terms of D_{6h} presented in the next section.

We refer to the new eigenstates as C_{6v} symmetrized, and denote by V_2 the unitary transformation *from* C_{3v}- *to* C_{6v}-symmetrized basis. The norms of its matrix elements are shown in Fig. 10.

We see that the transition from C_{3v} to C_{6v} leaves the ${}^{i}E_{3/2}$ states practically unaltered, as expected from Fig. 9. We also see that the pairs of $E_{1/2}$ quasidegenerate subspaces in C_{3v} (levels 5-6, 9-10, and 14-15) are remixed and given distinct symmetry labels in Fig. 12, as suspected. Finally, we see in the lower right corner of Fig. 10 three nondiagonal blocks mixing levels 11, 12, and 15 nontrivially together. The asymmetric structure might indicate that a level above level 15 should also have been included in the solution space. Block structures like this are useful in revealing nearby states of similar symmetry.

It has not yet been demonstrated that the elevated symmetry C_{6v} was a good approximation to the true solution of the original Schrödinger equation, therefore we show in Fig. 11 the energy shifts ΔE due to the imposed symmetry C_{6v}. One sees that they remain very small (<0.6 meV) compared to the confinement energies (max. 2.05% for level 4). Not surprisingly, they do, however, increase by an order of magnitude w.r.t Fig. 6. This is a clear manifestation that C_{6v} symmetry is not a true symmetry of the system and that *it is imposed*. Note also that C_{6v} symmetrization naturally tends to bring closer the newly intermixed energy levels, and the larger their original lack of degeneracy, the larger their final shift ΔE.

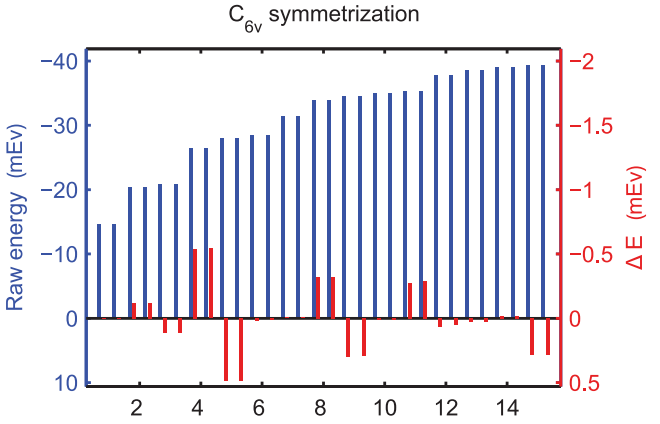

FIG. 11. (Color) Energy changes after C_{6v} symmetrization (for D_{6h} symmetrization see Table III). The raw energy spectrum is shown in blue, and the difference between symmetrized and raw spectrum is red (bright gray).

The weights of the C_{6v} double-group irreps for C_{6v}-symmetrized eigenstates are shown in Fig. 12. These double-group irreps subduce correctly towards the previous identification with C_{3v} (Fig. 7). The most interesting aspect of Fig. 12 is certainly that the first two levels which were characterized by $E_{1/2}$ C_{3v} irreps (levels 2 and 3) are now distinct C_{6v} irreps, with nearly pure character, similarly for levels 4 and 5. As the two latter levels were not as much degenerate, their energy change is much larger (Fig. 6). The same comment also applies to levels 8 and 9, although we see that these levels do *not* seem to be well described by the elevated symmetry. This is not surprising since higher-energy levels are generally more sensitive to symmetry-breaking contributions from the bulk crystal symmetry. For the lower levels, the remixed states are well defined by $E_{1/2}$ or $E_{5/2}$ irrep labels, accordingly they approximately obey the symmetry of the elevated symmetry groups.

The symmetry weights of the spinor components of the C_{6v}-symmetrized eigenstates are given in Fig. 13 (using only C_{3v} irreps, for easier comparison with Fig. 8). The single-group decomposition of the components of the ${}^{i}E_{3/2}$ states obviously

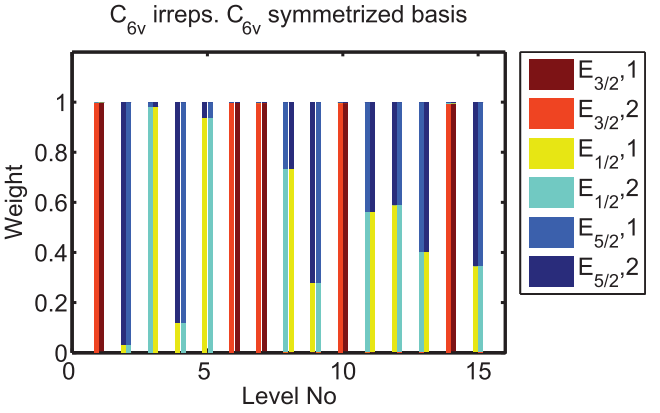

FIG. 12. (Color) Double-group weights $w_{\mu}^{\Gamma}(\overline{\psi}_{\mu}^{\Gamma})$ w.r.t. the C_{6v} irreps after C_{6v} symmetrization.

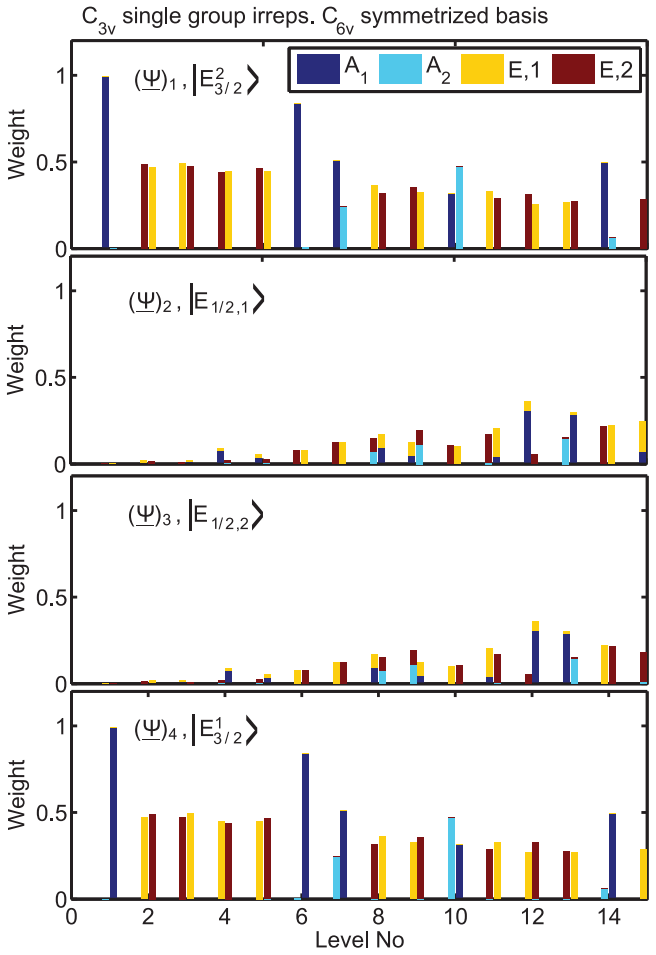

FIG. 13. (Color) Weights $w_\mu^\Gamma(\overline{\psi}_\mu^\Gamma)$ for each component of the HSBF basis, where Γ μ are single-group irreps and partner functions of the C_{3v} group. The eigenstates have been transformed using the C_{6v} symmetrization.

remains the same as in Fig. 8. It is more interesting to consider the $E_{1/2}$ states, especially those corresponding to levels 2 and 3, and also levels 8 and 9. The weight imbalance present in Fig. 8 has essentially disappeared in the new eigenstate basis (Fig. 13). This is a *meaningful numerical proof* that indeed there was a mixing between the quasidegenerate levels 2-3 (and 8-9) due to grid imperfections, not retrievable by C_{3v} symmetrization because these states bore identical irreps! In the elevated C_{6v} group the different irreps can be easily disentangled, for which the restoration of a correct balance is also a clear signature.

3. D_{6h} as the ultimate elevated symmetry?

Symmetry elevation towards C_{6v} or D_{3h} revealed to be very similar and of the same quality. This is a hint that D_{6h}, which collects all their symmetry elements, could be really relevant as the best approximate elevated symmetry group. In fact, this should not be entirely surprising since mesoscopic symmetry is D_{6h}, it was crystal symmetry which limited to C_{3v} at the microscopic level. PTCOallows to estimate these effects by testing D_{6h} symmetrization and giving figures of merit. To this end, *both* $\mathcal{C}_6$ and $\mathcal{S}_3$ are just added to CSCO and the τ_μ^Γ

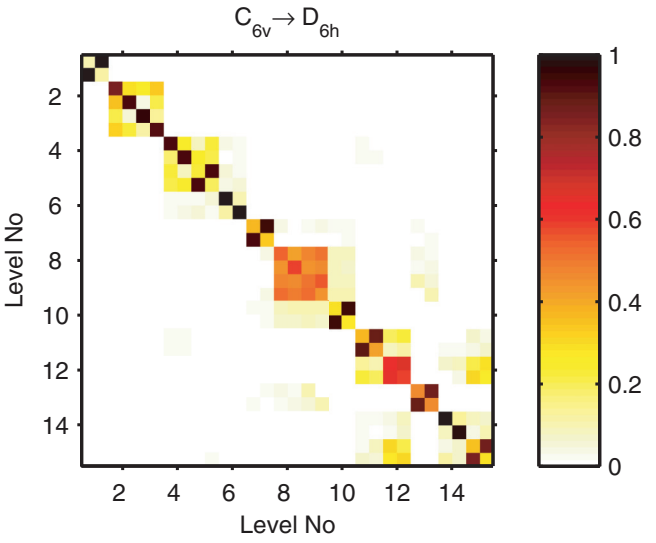

FIG. 14. (Color) Norms of the V_3 matrix elements, connecting the C_{6v}-symmetrized states to D_{6h}-symmetrized basis.

parameters were obtained by further slightly splitting by ± 0.1 the values of Table V for gerade/ungerade D_{6h} irreps (fine symmetry discrimination).

Figure 14 shows the norms of the elements of the unitary matrix V_3 transforming *from* C_{3v}- *to* D_{6h}-symmetrized eigenstates. Except for levels 8-9, 11-12, and 15 there are little changes (apart from trivial state reordering). Again, remixing of highest excited states is limited by the size of the solution space. Remixing of levels 8 and 9 can now be nicely and clearly interpreted by their distinct irreps $E_{3/2,u}$ and $E_{5/2,u}$ (both $E_{1/2}$ in Fig. 9). Again, the departure from D_{6h} symmetry becomes important after level 10, in particular for levels 11, 12, and 15 that have strongly mixed character: it is natural that excited states are more sensitive to symmetry breaking by the underlying zinc-blende lattice.

The energy shifts due to D_{6h} symmetrization are summarized in the columns of Table III and stay on the same order as for C_{6v}. The renormalization of energy differences between neighboring levels which bore $E_{1/2}$ labels in C_{3v} are not significantly larger than the corresponding values for C_{6v} (Fig. 11), demonstrating the real relevance of D_{6h} as the ultimate symmetry elevation. In the top plot of Fig. 15, the D_{6h} double-group weights of the symmetrized eigenstates are displayed. Their purities are very similar to what they were in the C_{6v} analysis (Fig. 9). D_{6h} symmetry is thus fulfilled approximately to the same degree as C_{6v} or D_{3h}, but many more kinds of symmetries are discriminated, as evidenced by Fig. 15.

The four bottom plots of Fig. 15 show the single-group analysis of each spinorial component in the D_{6h} HSBF basis which will find application in the next section. The reader can check that these numerical results are in fair agreement with the analytically predicted D_{6h} UREFs, predicted in Appendix section 3.

We have here fully confirmed the relevance of D_{6h} approximate symmetry elevation in the valence band for our structure, including when it applies and when it has limitations.

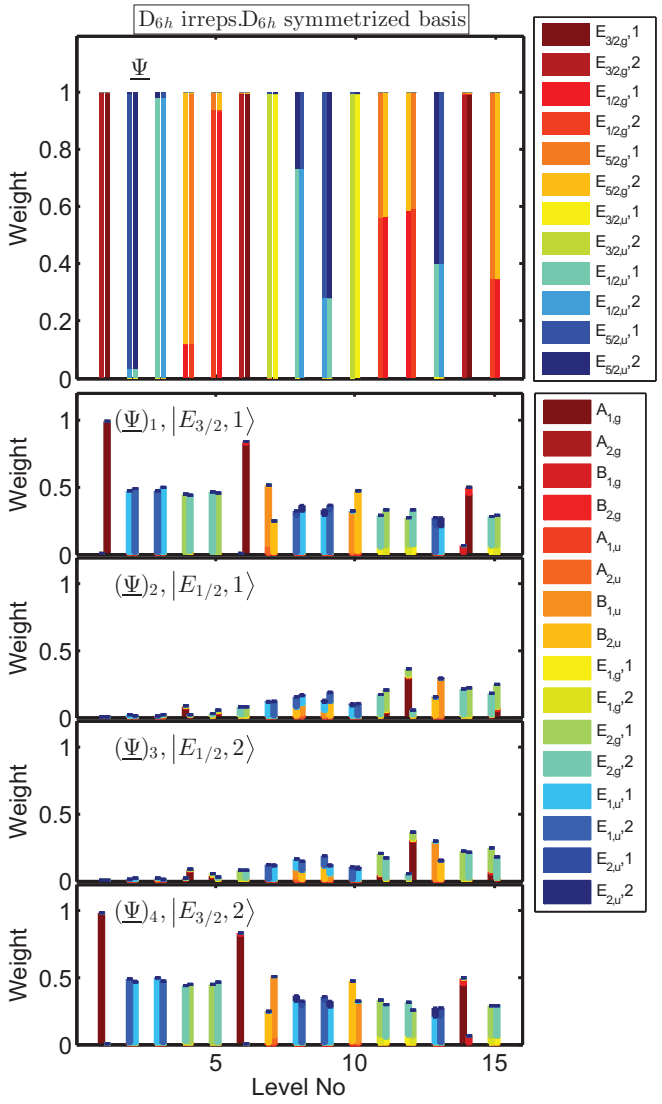

FIG. 15. (Color) Double-group weights (top plot) and single-group weights (four lower plots) for each HSBF component w.r.t. D_{6h} group, using the D_{6h}-symmetrized basis.

D. Characterization of DPGPS, UREFs, and envelope function symmetry of valence band eigenstates

Up to now we have mainly concentrated on eigenstates as a whole. It is, however, possible to get important information by looking closer into the spinorial components, by studying the nature of the UREFs, and identifying dominant HSBF (DPGPS), as well as dominating UREF. Such an approach will not only provide enhanced physical interpretation and intuition, but can also prove to be extremely helpful information when building more complex objects, e.g., multiexcitons in a configuration interaction approach and in the strong confinement limit (cf. Refs. [9,31]).

The analysis will be carried out using essentially elevated D_{6h} symmetry which provides the finest classification, determining DPGPS in Sec. VI D 1 and dominant UREF's in Sec. VI D 2. It is then completed in Sec. VI D 3 by searching classical azimuthal and radial quantum numbers, which will provide an intuitive understanding for the irrep sequence and outline a link to symmetry-adapted functions [27].

The main results of this section are summarized in Table III. Together with Fig. 15, it provides the finest understanding of all valence band states and is the only way to decipher completely the remarkable properties of the optical transitions.

1. *Heavy and light hole mixing, HSBFs, and DPGPS*

The most common way to analyze VB states in heterostructures is in terms of valence band mixing between HH and LH states. This is an import from quantum well physics where there is no mixing at zone center. In strongly oblate disklike structures (cf. Fig. 1) this remains a good starting point due to weak mixing for the ground states, allowing to deduce that the ground state should be HH-like. Moreover, one can coarsely predict the order of excited HH- and LH-like states using a scalar anisotropic effective mass model based on Eq. (3.4) which neglects valence band mixing and assumes an infinite cylindrical potential well with the same height and cross-sectional area as the nanowire QD. This yields a separation of about 45 meV between the ground HH and LH states. Accordingly, we do expect the 15 lowest-energy levels (Table III) to be dominated by HH states, in agreement with what can be seen in Figs. 8 and 15, where the HH weight always remains above 0.5. We also see clearly in Figs. 8 and 15 that the degree of band mixing increases with the excitation levels. It is very low for the ground state, which is nearly a pure (99%) HH state. Band mixing starts to be significant above level 6.

Here, a powerful way to analyze VB states called "HSBF valence band mixing" is proposed. It helps to identify, whenever possible, the DPGPS, i.e., the dominating HSBF. As the first 15 Kramers conjugate pairs are HH-like, their C_{3v} DPGPS is logically always $|E^i_{3/2}\rangle$, $i = 1,2$, and $|E_{3/2,g}\rangle$ in D_{6h} (cf. Appendix section 2). This concept, together with information on the dominating UREF, is important, and will enable in the next section to find the deep reason for all the observed quasidegeneracies.

2. *Analysis of UREFs*

Let us first identify for every level (Kramers' pair) the dominant UREFs, using Fig. 15. We find the following dominances: levels 1, 6, and 14 are $A_{1,g}$, levels 2, 3, 8, 9, and 13 are $E_{1,u}$, levels 4, 5, 11, 12, and 15 are $E_{2,g}$, level 7 is $B_{1,u}$, and level 10 is $B_{2,u}$. This is summarized in column 6 of Table III. Column 4 (for C_{3v}) can be obtained by subduction. Note that we have regrouped some levels together as pairs in this enumeration; the reason will become clear during the forthcoming analysis.

Our first purpose is to show that a description of the states in terms of product states between the dominant UREF and DPGPS allows to explain most of the level sequence. Indeed, the double-group irrep of each level (or the irrep pair in case of a level pair) can be faithfully generated by making the following irrep products: for the isolated levels 1, 6, and 14 $A_{1,g} \times E_{3/2,g} = E_{3/2,g}$, for the level pairs 2, 3 and 8, 9 $E_{1,u} \times E_{3/2,g} = E_{5/2,u} + E_{1/2,u}$, for level pairs 4, 5 and 12, 15 $E_{2,g} \times E_{3/2,g} = E_{5/2,g} + E_{1/2,g}$, for level 7 $B_{1,u} \times E_{3/2,g} = E_{3/2,u}$, for level 10 $B_{2,u} \times E_{3/2,g} = E_{3/2,u}$, for level 11 $E_{2,g} \times E_{3/2,g} = E_{1/2,g}$ $(+E_{5/2,g}$ but the latter

is missing), and finally for level 13 $E_{1,u} \times E_{3/2,g} = E_{5/2,u}$ ($+E_{1/2,u}$ but the latter is missing). The missing levels related to level 11 and to level 13 are likely to lie above the 15th energy level. The association of level 12 (instead of 11) with level 15 will be explained in the next section when looking at azimuthal and radial quantum numbers. It is still an open question whether the departure from D_{6h} symmetry of levels 11, 12, and 15 may be further minimized by including the missing partner of 11 in the symmetrization procedure (cf. Fig. 14).

The pairwise clustering in energy for levels (2, 3) and (4, 5) and (8, 9) and (12, 15) (see Fig. 11 and Table III) can also be very clearly explained by dominant product states. It should be kept in mind that the quasidegeneracies of (4, 5) and (12, 15) with 6 and 13 and 14, respectively, are *accidental* with respect to D_{6h} since these have different symmetries. While the energy of the lower pairs is closely packed together due to negligible valence band mixing, higher pairs like (8, 9) and (12, 15) become more and more significantly split apart. The splitting is, however, already visible for the level pair (4, 5), manifested in Fig. 15 as nonvanishing weight in the central $E_{1/2}$ components in which there are distinct UREFs for the respective levels. This is a clear demonstration that band mixing can also be a relevant concept in the HSBF picture ("HSBF band mixing").

The isolated levels 1 and 6 and 14 are all linked with the dominating $A_{1,g}$ UREF. Although it is customary that the fundamental level is strongly dominated by a fully invariant envelope function concentrated in the DPGPS component, the structure of levels 6 and 14 can again only be explained in the next section when looking at azimuthal and radial quantum numbers. Note that level 14 also displays contributions from other HSBF components.

Levels 7 and 10 are also interesting. They are very similar and form in a way a complementary pair because the relative strength of the weights of B_{1u} and B_{2u} is opposite between the two levels. In fact, within one level neither of the two is strongly dominant, but this is allowed by symmetry since the two products $B_{1,u} \times E_{3/2,g}$ and $B_{2,u} \times E_{3/2,g}$ give both of them global $E_{3/2,u}$ symmetry. In contrast with the partners of an $E_{1,u/g}$ or $E_{2,u/g}$ irrep (see Fig. 15) which must be always balanced as predicted by the Wigner-Eckart theorem, the weights of the B_{1u} and B_{2u} UREFs must not necessarily be balanced in these levels. Levels 7 and 10 therefore illustrate the general fact that *even if a state has a clear DPGPS* (clearly dominant HSBF), *it may not necessarily have a single very dominant UREF*, as allowed by the analytical UREF decompositions given in Appendix section 3.

Thus far, we have only considered the DPGPS components of the spinors. The higher excited levels also have a significant contribution from the $E_{1/2}$ HSBFs (LH). For simplicity, we discuss this only in C_{3v} symmetry. First, note that all E-partner functions within LH components have balanced (equal) weight despite band mixing: this is indeed imposed by symmetry [cf. Eq. (4.3)]. By contrast, and in analogy to the discussion of the previous paragraph, level 13 has A_i, $i = 1,2$, UREF pairs in the LH components with an allowed weight imbalance. Second, we have analytically demonstrated that time-reversal symmetry imposes restrictions on the LH components of the $E_{1/2}$ states [cf. Eq. (4.4)]. As a clear example, let us consider the first pair of $E_{1/2}$ states with significant LH weights, levels 8 and 9, which contain all UREFs predicted by Eq. (4.3), as can be seen in Fig. 9. We have been able to check numerically that the relative phase of the A_1 and A_2 UREFs do indeed differ by a factor i compared to the E UREFs, in agreement with Eq. (4.4). Level 12 has a rather large A_1 LH component; we do not think, however, that this state should be identified with a ground LH-like state.

Finally, it is interesting to consider the parity of the dominant UREFs found with respect to the σ_h operation. From the D_{6h} character table it is easy to see that all the single-group irreps of the dominant UREFs appearing so far, namely, $A_{1,g}$, $A_{2,g}$, $B_{1,u}$, $B_{2,u}$, $E_{2,g}$, and $E_{1,u}$, are even under σ_h [nevertheless, it should be noted that non-dominant UREFs demonstrate some level of z excitation due to band mixing (cf. Fig. 15)]. The reason for this behavior of the dominant UREFs is rooted in the high lateral to axial aspect ratio of the QD under consideration which is 40:5. We therefore expect the envelope functions of the levels considered here to have excitations mainly in the transverse plane.

To conclude, we would like to stress that the dominant UREFs that have been identified in this section will play a key role in enabling (1) a further analysis of transverse plane excitations in terms of azimuthal and radial quantum numbers, and (2) a further interpretation of respective oscillator strengths in optical spectra.

3. *Approximate azimuthal and radial quantum numbers: The role of symmetry-adapted functions*

The goal of this section is to investigate the correspondence between a classical effective mass analysis for a disk-shaped quantum dot in terms of standard azimuthal and radial quantum numbers, and the sequence of irreps for the dominating UREFs identified in the previous section. A logical ordering of the level sequences in terms of azimuthal and radial quantum number can be also viewed as *approximate symmetry elevation to* $D_{\infty h}$.

The Schrödinger equation for a circular disk-shaped QD with infinite barriers is separable in azimuthal and radial coordinates, and leads to eigenfunctions proportional to products of an azimuthal exponential $\exp(im_a\phi)$ with an l_ath-order Bessel function $J_{l_a}(k_{l_a,n_r}r)$ for the radial coordinate, where it is understood that $k_{l_a,n_r}R$ is the n_rth zero of J_{l_a} with R being the dot radius. They are labeled by the azimuthal and radial quantum numbers $l_a = 0,1,\ldots,\infty$ and $n_r = 1,\ldots,+\infty$. In cylindrical coordinates, m_a is restricted to $m_a = \pm l_a$ (and axial excitations would be labeled by n_z). The number of azimuthal nodes is thus l_a, and there is a twofold degeneracy for states with $l_a \neq 0$.

Similar approximate quantum numbers are to be expected in our nearly cylindrical 3D solutions (see Fig. 4 for the conduction band and Fig. 16 for the valence band spinor component cross sections). Therefore, we shall in the following specify the character of the computed dominating UREFs not only by their irreps, but also by additional subscripts $\psi^{\Gamma}_{n_a,n_r}$ where n_a and $(n_r - 1)$ specify the number of nodes in azimuthal and radial direction, respectively (when they can be determined). The subscripts were identified by visual inspection for the first 15 levels, and are listed in the last column of Table III.

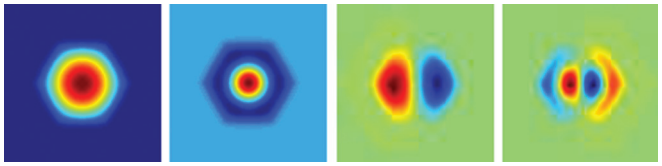

FIG. 16. (Color) Cross sections of a selection of the contributions to the valence band spinor. The envelope functions exemplify no lateral excitation as well as lateral excitation in radial and/or azimuthal direction.

We now consider in detail the energy-level sequences. First, the sequence of levels 1, 6, and 14 with dominating UREF of $A_{1,g}$ symmetry: it is easy to see that they nicely form the sequence of $m_a = 0$ levels with $n_r = 1,2,3$, i.e., purely radial excitations.

Next, another less trivial, but fundamental, sequence is the $n_r = 1, l_a = 1 \ldots 5$ sequence. We recognize the following five level pairs: (2, 3), (4, 5), (7, 10), (11, missing partner), and (13, missing partner). The question is now how to obtain further confirmation of this sequence. If one looks at the subduced representations from O(3), the so-called symmetry-adapted functions (SAFs), listed in Tables T35.5 and T35.6 of Ref. [27], we can confirm that the link is correct, as the SAF quantum numbers l,m, here corresponding to l_a,m_a, are in agreement with the appropriate single-group labels. One finds that the $l = 1$, $m = \pm 1$ basis subduces to $E_{1,u}$ in D_{6h} symmetry; $l = 2$, $m = \pm 2$ subduces to $E_{2,g}$; $l = 3$, $m = \pm 3$ subduces to $B_{1,u} + B_{2,u}$; $l = 4$,$m = \pm 4$ subduces to $E_{2,g}$; and, finally, $l = 5$, $m = \pm 5$ subduces to $E_{1,u}$. Hence, we have confirmed that this sequence of azimuthal excitations is in agreement with the sequence of irreps for the dominating UREFs, and additionally that levels 11 and 13 do have missing partners which must be at higher energies. For level 11, this was also indicated by the structure of the intermixing blocks in the lower right corner of Fig. 15 as previously mentioned. Similarly, we can identify the last $n_r = 2$, $l_a = 1,2$ sequence corresponding to level pairs (8, 9) and (12, 15). Again, the corresponding l,m quantum numbers subduce to the correct irreps $E_{1,u}$ and $E_{2,g}$, respectively.

Even further interpretation is sometimes permitted. Let us return to the pair of levels (7, 10). Three nodal planes here correspond to either $B_{1,u}$ or $B_{2,u}$ symmetry. These are distinguished by a rotation by $\pi/6$ of the nodal planes. In our choice of coordinate system (Fig. 1), the $\psi_{31}^{B_{1,u}}$ functions have nodal planes perpendicular to the facets of the hexagon, whereas the $\psi_{31}^{B_{2,u}}$ have nodal planes intersecting the corners of the hexagon. These two orientations give rise to different filling factors. The $\psi_{31}^{B_{1,u}}$ functions fill the area of the hexagon more effectively than the corresponding functions with $B_{2,u}$ labels. The curvature, and thus the energy, is therefore higher for the $\psi_{31}^{B_{2,u}}$. This is also seen in the conduction band, where there is a splitting between the two corresponding levels (CB levels 7 and 8). For the valence band, the spinors contain mixtures of $\psi_{31}^{B_{1,u}}$ and $\psi_{31}^{B_{2,u}}$. Energy level 7 has $B_{1,u}$ as the largest contribution and a smaller contribution of $B_{2,u}$. The situation in energy level 10 is mirrored. The energy splitting between the levels is mostly due to the different curvature of $\psi_{31}^{B_{1,u}}$ and $\psi_{31}^{B_{2,u}}$. Note that the different curvature of states rotated by $\pi/4$ also applies for the E_1/E_2 states with azimuthal excitations. However, for these states unequal weight in the UREF partners would violate the restrictions from Wigner-Eckart theorem.

As valence band mixing is weak for the lowest-energy levels, the corresponding dominant HH envelopes will not hybridize with LH components. The lowest-order UREFs observed in the LH components are $\psi_{31}^{B_{i,u}}$, $i = 1 \ldots 2$, envelope functions. This further supports our previous assumption regarding the DPGPS as there is no sign of an LH-like sequence.

The considerations of this section can also be carried out for the simpler conduction band; we leave this as an exercise for the reader. The situation in the valence band is much more complicated due to direction-dependent effective masses and valence band mixing. We expect that the approach also works when sequences of vertically excited states occur, and with $E_{1/2,g}$ DPGPS states (LH-like).

At this stage, Table III entails the full information for a complete classification of all states in compact form, both in true C_{3v} symmetry and in elevated D_{6h} symmetry. Note that the energy deviation due to symmetrization is the same in D_{6h} as in C_{3v} for the states labeled $E_{3/2,g}$ and $E_{3/2,u}$ (D_{6h}). Also note that in D_{6h}, the energy deviation is almost balanced within one pair. The last column of the table summarizes also the azimuthal and radial properties of the dominating UREF. In Table II, we present a similar summary for the conduction band states.

VII. OPTICAL TRANSITIONS

Sharp optical transitions in quantum dots are among their major attractive features for device applications. In this work, we now show that when the identification of the dominant UREF can be performed, one obtains further clues to the oscillator strength spectrum. When azimuthal and radial quantum numbers can also be identified, even further constraints are revealed. As a result, the presence of main lines can be explained, and fine structure can be interpreted.

It is well known that the oscillator strength corresponding to each interband d-polarized transition ($d = x,y,z$) at frequency $\hbar\omega = E_{n_c}^{\Gamma_c} - E_{n_v}^{\Gamma_v}$ is proportional to the summed squared $c - v$ interband matrix element $\bar{M}_{d,n_c,n_v}(\Gamma_c,\Gamma_v)$, where the sum is over the degenerate contributing states, and can be written

$$\bar{M}_{d,n_c,n_v}(\Gamma_c,\Gamma_v) = \sum_{\Gamma_c'}{}' \sum_{\Gamma_v'}{}' \sum_{\mu_c,\mu_v} |\langle \psi_c : n_c,\Gamma_c',\mu_c | P_d | \psi_v : n_v,\Gamma_v',\mu_v \rangle|^2. \tag{7.1}$$

The primed sum denotes a sum over eventually conjugated contributions, i.e., Γ' summed over $\{\Gamma,\Gamma^*\}$ only if $\Gamma \neq \Gamma^*$. In Eq. (7.1), ψ_c and ψ_v denote full conduction and valence band kets corresponding to energy levels $E_{n_c}^{\Gamma_c}$ and $E_{n_v}^{\Gamma_v}$, respectively.

For the symmetry groups considered here, the set of momentum operators P_d, $d = x,y,z,$, can be divided into two distinct irreducible tensor operator (ITO) sets. In C_{3v}, one has [27]

$$\{P_x,P_y\} \leftrightarrow \left\{P_\mu^E,\mu = 1,2\right\}, \quad P_z \leftrightarrow P^{A_1} \tag{7.2}$$

TABLE VI. Optical transition anisotropy ratios A_{zx} for QD's with C_{3v} symmetry, here describing transitions from conduction band states Γ_c to valence band states Γ_v.

	$\Gamma_v = {}^iE_{3/2}$	$\Gamma_v = E_{1/2}$
$\Gamma_c = {}^iE_{3/2}(E)$	1	-1
$\Gamma_c = E_{1/2}(E)$	-1	$f(\psi_c^E,\Phi_v^E,\phi_v^E)$[a]
$\Gamma_c = E_{1/2}(A_i)$	-1	$\frac{3}{5}$

[a] $f(\psi_c^E,\Phi_v^E,\phi_v^E) = \frac{\frac{2}{3}|\langle\psi_c^E|\Phi_v^E\rangle|^2 - |\mathrm{Re}\langle\psi_c^E|\phi_v^E\rangle|^2}{\frac{2}{3}|\langle\psi_c^E|\Phi_v^E\rangle|^2 + |\mathrm{Re}\langle\psi_c^E|\phi_v^E\rangle|^2}$.

and in D_{6h}

$$\{P_x,P_y\} \leftrightarrow \left\{P_\mu^{E_{1,u}},\mu=1,2\right\}, \quad P_z \leftrightarrow P^{A_{2,u}}. \tag{7.3}$$

These correspondences allow to apply the generalized Wigner-Eckart theorem for evaluating the inner matrix element $\langle\psi_c : n_c,\Gamma_c,\mu_c|P_d|\psi_v : n_v,\Gamma_v,\mu_v\rangle$. This leads to the prediction of optical oscillator strength isotropy in the x-y plane [23], and allow to use group theoretical selection rules for optical transitions.

It should be stressed that the decomposition into UREFs linked with the HSBF basis allows to go beyond the simple use of the Wigner-Eckart theorem. Indeed, the UREFs lead straightforwardly to the prediction of "magic ratios" in polarization anisotropy [23], in the frame of our Luttinger model, and a conduction band *with no spin splitting*. At this point, the full conduction band spinors must be reconstructed, as described in Ref. [23]. In the case of C_{3v} symmetry, four types of Kramers degenerate pairs then appear: $E_{1/2}(A_1)$ and $E_{1/2}(A_2)$ for conduction band states with A_1 and A_2 envelopes, respectively, and $E_{1/2}(E)$ and $E_{3/2}(E)$ for states with E envelopes. The latter two are always degenerate. The polarization anisotropy, defined as $A_{ij} = (\bar{M}_i - \bar{M}_j)/(\bar{M}_i + \bar{M}_j)$, $i,j \in \{x,y,z\}$, can hence be calculated using UREFs, and reveals the magic anisotropy ratios A_{zx} given in Table VI. The ratios ± 1 in Table VI stem from standard C_{3v} selection rules. The Wigner-Eckhart theorem also predicts $A_{xy} = 1$ and $A_{zy} = A_{zx}$ for all irreps.

Table VI also evidences that the polarization anisotropy ratio cannot be analytically predicted for $E_{1/2}(E) \to E_{1/2}$ type transitions.

A. Numerical calculation of C_{3v} optical oscillator strengths

Calculated optical oscillator strengths for the nanowire QD levels listed in Tables III and II are displayed as a function of the transition frequency in Fig. 17. We used D_{6h}-symmetrized valence band states in order to interpret the optical spectra in most details. In the side figure, the details of two transitions calculated in the C_{3v}-symmetrized basis are also displayed; other differences were minor. By contrast, for the conduction band we used the raw calculated states since these states were already sufficiently symmetrized, rendering unnecessary a further D_{6h} symmetrization. Nevertheless, we did restore in Fig. 17 an exact degeneracy for E conduction band states, for the purpose of clarity of the fine structure in the figure. The numerical splitting of the computed energies was anyway below the estimated convergence (Sec. VI A).

The upper subplot in Fig. 17 shows the total oscillator strengths for the main transitions (summed over all polarization directions), while the lower subplot shows the corresponding A_{zx} anisotropy ratios. It must be understood that other effects also occur in a real experiment, aside from the neglected Coulomb contributions. This may to some extent change the predicted spectrum; in particular, there are important effects in nanowires due to the high index contrast between the wire and the surroundings [35] (dielectric mismatch effect). Nevertheless, the oscillator strength spectra given by single-particle calculations as in Fig. 17 are often the main characteristic of the intrinsic optical response of QDs.

We now apply the theory to study in detail the oscillator strengths of each optical transition, which is color coded in Fig. 17. They are numbered so that the properties of the conduction band level i and valence band level j corresponding to transition CBi-VBj can be directly read off using the previously obtained Tables III and II, and Eqs. (7.2) or (7.3).

B. Dominant and missing optical transitions

A first striking feature of the upper part of Fig. 17 is the dominant diagonal character of the optical transitions, i.e., CBi-VBj is most intense for $i = j$ (the irrelevant numbering within degenerate CB levels, was explicitly chosen to respect CBi-VBj diagonality). This diagonal character is nearly perfect for the ground-state transition, as well as for the first pair $i = 2,3$, but progressively weakens as one climbs the excitation ladder.

It is also clear that the highest pairs give rise to a richer structure with side peaks due to the valence band complexity, but still the (CB7,CB8) pair is dominantly diagonally coupled to the (VB7,VB10) pair, and (CB9,CB10) to (VB8,VB9) pair (see Table III). Cross-coupling-like CB7-VB10, etc., also appear as sub-structures within these dominant pairs.

Looking back to the analysis of the corresponding states in Tables III and II, we find that symmetry elevation to D_{6h} is an important ingredient to explain missing nondiagonal transitions in Fig. 17. However, not all of them are explained. Take, for example, the set of transitions from the ground conduction band level CB1-VBj. Only CB1-VB1 is observed. In principle, using double-group selection rules in C_{3v}, all values of j are permitted from CB1 in x-y polarization, but in D_{6h} only $j = 1,5,6,11,12,14$ are permitted. In z polarization, $j = 2$–$5,8,9,11$–$13,15$ are permitted in C_{3v} while only $j = 5,11,12$ would be in D_{6h}. Thus, symmetry elevation accounts for part of the missing transitions, but obviously it is not enough to explain all of them.

However, for the lowest-energy states all missing transitions can be explained if one considers in addition *both* the symmetry of the dominant UREF and the presence of the approximate azimuthal and radial quantum numbers. This is particularly clear with the set CB1-VBj. First, on the basis of the symmetry of the dominant UREF $A_{1,g}$ of CB1 and the contributing UREFs of VBj, all z-polarized lines are forbidden, and only $j = 1,6,14$ are allowed in x-y polarization. Second, to explain the remaining missing lines from CB1, corresponding to $j = 6,14$, it suffices to invoke the *approximate* selection rule based on the radial quantum number of the dominant UREF,

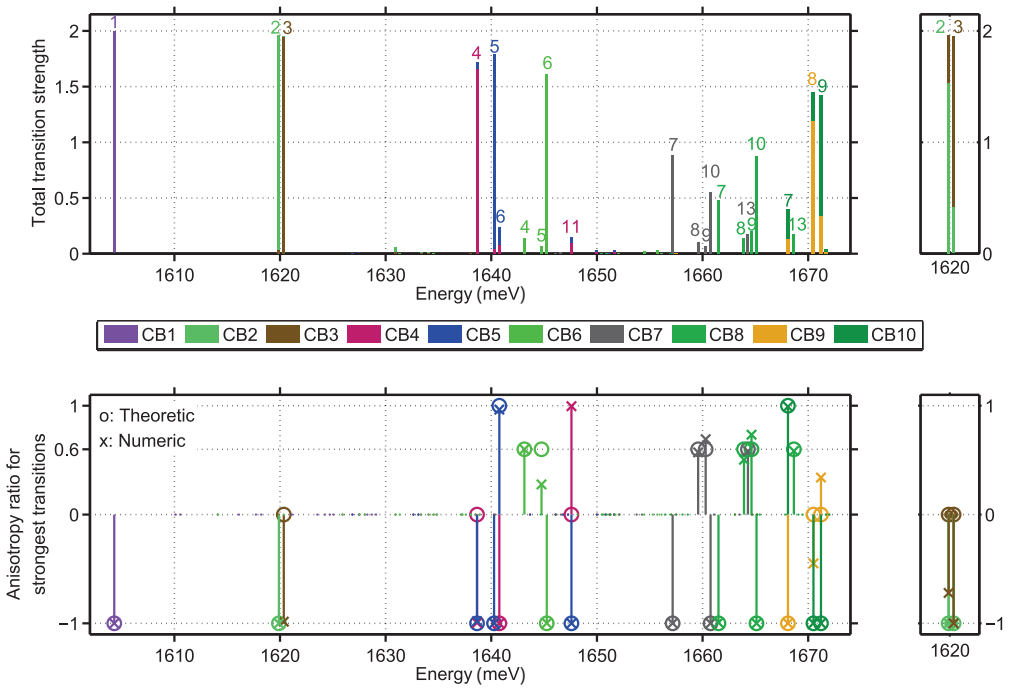

FIG. 17. (Color) The top subplot shows the combined optical oscillator strength $\bar{M}_x + \bar{M}_y + \bar{M}_z$ as a function of energy. The colors label the contributions due to the individual conduction band levels, and the valence band state number is indicated by numbers. The lower subplot shows the anisotropy ratios A_{zx} for the significant transitions (limit set to $\bar{M}_x + \bar{M}_y + \bar{M}_z = 0.05$). The theoretical anisotropy ratio predictions for C_{3v} are also included. Some of the anisotropy ratios cannot be predetermined; for these transitions, the theoretical value has been set to the dummy value 0 to mark them. The interested reader may recover the separate results in each direction using the analytical results $A_{xy} = 1$ and $A_{zy} = A_{zx}$, whose validity was also confirmed numerically. The insets at the right show the CBi-VBj, $i, j = 2,3$, in the C_{3v} basis.

which is $n_r = 1$ for CB1, and $n_r = 2,3$ for VB6 and VB14, respectively (see Tables III and II).

Let us examine more closely the optical coupling between diagonally coupled pairs in view of the UREFs. In (CB2,CB3) − (VB2,VB3), symmetry elevation to $D_{6h}$is not sufficient to predict only CB2-VB2 and CB3-VB3 transitions as observed in Fig. 17. In this respect, it is interesting that if one assumes C_{3v} symmetry, both the crossed transitions between the pairs (CB2-VB3 and CB3-VB2) should appear. Indeed, this is what we observe in the spectrum calculated in the C_{3v}-symmetrized basis (see side of Fig. 17). The observation of CB3-VB2 would witness the D_{6h} symmetry breaking present in the [111] Luttinger Hamiltonian, and might well be resolvable experimentally, while CB2-VB3 would be compatible with both symmetries.

In the higher diagonally coupled pairs (CB4, CB5)-(VB4, VB5) and (CB9, CB10)-(VB8, VB9), the same effects are observed and the same considerations apply. For these two sets of transitions, we also see in Fig. 17 the appearance of additional nondiagonal transitions with other levels, a trend which naturally increases with transition energy. The last diagonally coupled pairs (CB7,CB8)-(VB7,VB10) are particularly interesting because the two electronic levels CB7 and CB8 are nondegenerate, hence, in Fig. 17 one observes four dominant peaks for these transitions.

C. Optical anisotropy of dominant transitions

The optical anisotropies are also of fundamental interest. By contrast to the selection rules discussed in the previous section, nearly all optical anisotropies can be explained in C_{3v} symmetry. Table VI, with the help of the classification of Tables III and II, predicts the anisotropy ratio to be -1 for transitions between isolated levels CBi-VBi, $i = 1$ or 6, in agreement with the lower part of Fig. 17.

The transitions between the coupled pairs (CB7,CB8) and (VB7,VB10) are also predicted to have anisotropy ratio -1, as is well verified numerically. However, the situation for the other diagonally coupled pairs is more subtle.

In (CB2,CB3)-(VB2,VB3), the optical anisotropy is predicted to be undetermined for the two transitions stemming from CB3, and -1 for the two stemming from CB2. This is satisfied in the C_{3v}-symmetrized basis (see side of Fig. 17), but the anisotropy of both, particularly CB3-VB3, is still close to -1. The explanation is very simple if one recalls that the LH weight in VB2 and VB3 is less than 4% (from Table VI, the undetermined anisotropy ratios will be close to -1 if the overlap with Φ_v^E vanishes). The departure from -1 is much bigger for CB3-VB2, which can be understood by recalling that this transition should in fact be forbidden in the x-y polarization in D_{6h}. Hence, it is more sensitive to LH admixture. We should point out that the disappearance of the transition CB2-VB3 in the D_{6h}-symmetrized basis, evidenced in Fig. 17, cannot be understood on the basis of D_{6h} symmetry alone. We suspect that a study generalizing the magic ratios to D_{6h} symmetry, linked with the neglect of conduction band spin splitting, might explain this observation, but the analytical verification would be quite overwhelming.

The optical anisotropy of (CB4,CB5)-(VB4,VB5) and (CB9,CB10)-(VB8,VB9) is entirely similar to

(CB2,CB3)-(VB2,VB3), but with the role of the two conduction and valence band levels reversed. Finally, the undetermined anisotropy ratios in transitions from CB9 to (VB8,VB9) depart more significantly from any specific values, as is expected due to increased band mixing.

D. Fine structure due to valence band mixing

Surrounding the series of dominant peaks, there is a particularly interesting fine structure produced by valence band mixing. This really starts to be significant for the set of transitions CBi-VBj with $i, j \geqslant 4$.

From the pair (CB4,CB5), weak additional transitions to VB6 and VB11 are visible in Fig. 17. From the Wigner-Eckart theorem, both the transitions to VB6 are allowed in elevated symmetry D_{6h} while towards VB11 only CB5-VB11 is allowed. We conclude that CB4-VB11 is a manifestation of the true C_{3v} dot symmetry. These weak transitions are slightly more intense in the z direction. The anisotropy ratios for the transitions CB4-VB6 and CB5-VB11 are -1, and for CB5-VB6 it is $+1$, in agreement with C_{3v} symmetry (Table VI). For the remaining CB4-VB11 transition, the undetermined anisotropy ratio proves numerically to be close to $+1$. Looking at the corresponding $E_{2,g}$ UREFs in the spinors [Eqs. (A13c) and (A13d)], we can confirm that both $+1$ transitions *are purely due to valence band mixing* since only the $E_{1/2,g}$ HSBF (LH components) can couple to CB5.

Aside from the next dominant transition CB6-VB6, we can see two weak transitions CB6-VB4 and CB6-VB5 in Fig. 17. Again, both transitions are due to valence band mixing, and are not predicted in elevated symmetry D_{6h}; they manifest the true C_{3v} symmetry of the QD. The novelty here is that both transitions should have the "magic" anisotropy ratio $\frac{3}{5}$ predicted by Table VI. This is very well satisfied by CB6-VB4, but CB6-VB5 displays a numerical anisotropy ratio close to 0.3 which will represent the largest deviation from the predicted value in our numerical data. Since its oscillator strength is rather weak, we can safely attribute this deviation to imperfect C_{3v} symmetrization.

Let us now investigate the weak transitions from the (CB7,CB8) pair to levels VBj, $j = 8,9,13$. These six transitions due to valence band mixing again manifest the true C_{3v} symmetry of the QD, and display quite accurately the "magic" anisotropy ratio $\frac{3}{5}$ for $E_{1/2}(A_1) - E_{1/2}$ transitions.

The last weak transitions in Fig. 15 are related to the highest excited pair (CB9,CB10) towards VB7 and display polarization anisotropy ratios of $+1,-1$, respectively. The symmetry considerations are the same as for (CB4,CB5) to VB6 (but correspond to a higher radial excitation), so they are both allowed in D_{6h} symmetry, and CB9-VB7 is a LH transition purely due to valence band mixing.

E. Summary of optical transition spectrum

Optical transitions with polarization perpendicular to the nanowire axis are clearly more dominant for the lowest-energy states. This is expected due to the oblate (quantum-well-like) aspect ratio of the QD (Fig. 1). The transitions with optical activity polarized along the nanowire axis are linked with valence band mixing and overlap between the conduction band and the LH components. Accordingly, we see an increasing number of transitions with this polarization for higher levels, as the valence band states become increasingly LH-like (see Table III). A computation with more energy levels, or a narrower QD with stronger lateral confinement, would have allowed to reach the ground LH-like level with strong dominance of z-polarized optical transitions. Our approach would then evidence the second kind of DPGPS. If the QD aspect ratio would be reversed to prolate, a reversal of the roles of HH and LH is expected.

Excitonic effects, which we have neglected in this work, are not expected to change this global picture of polarization anisotropy very much. It would introduce electron-hole exchange effects which would split all the dominant transitions into a further observable fine structure (which can be seen as quadruplets due to spin degeneracy). The symmetries of the fine-structure excitons can be easily obtained by the product of irreps [31]. Sometimes, doublets may remain, other times all lines would split in D_{6h}.

VIII. CONCLUSION

We have presented a systematic procedure based on class operators for symmetry analysis of the electronic states of a QD. The procedure, called PTCO, is based on postprocessing and alleviates the need for a code specialized with respect to a given symmetry (which would, however, feature significant gains in memory/time [36]). PTCO has been demonstrated using the $k \cdot p$ method for the conduction and valence bands of hexagonal GaAs QD grown within $Al_{0.3}Ga_{0.7}As$ nanowires. The high D_{6h} symmetry of the QD heterostructure is partly broken by the C_{3v} crystal symmetry carried by the Luttinger Hamiltonian, and by the unsymmetric computing grid. Using the PTCO on the computed results, we have been able to sort all these symmetry-breaking effects, and quantify them. We have demonstrated that the numerical grid effect was small and could be compensated by PTCO, while the deviations from the approximate elevated D_{6h} symmetry towards the true C_{3v} symmetry, albeit small, could be measurable.

The PTCO is simple to program, intrinsically systematic and automatized, and is carried out in a single step for a given symmetry, delivering at the same time symmetrized states with corrected energies and a classification for all quantum states. It is flexible, applies independently of the method used to compute the electronic structure, and can be tuned with very little efforts to analyze a higher symmetry in a next run. This enabled us to investigate the symmetry of each state, and its proximity to an elevated symmetry.

All the quantum states were analyzed to give quantitative weights for every symmetry group, for every ultimately reduced envelope function present in every spinorial component. We could then verify all analytical predictions made concerning the UREFs in the elevated D_{6h} symmetry. This approach allowed to identify dominant DPGPS and dominant UREFs for all states considered.

The analysis of the dominant UREFs opened the possibility to attribute additional azimuthal and radial quantum numbers to every state which can be viewed as a symmetry elevation effect to D_{6h}. Although approximate, the natural sequence

allowed to explain the order of irreps in the computed results, by subduction from $O(3)$ to D_{6h}.

A summary of the classification is given for all valence band states in Table III, and for all conduction band states in Table II. The classification provides insights into the origin of degeneracies and quasidegeneracies, and allows to predict all selection rules and most of the polarization properties. The information can also be used to construct approximate product states, relevant for the interpretation of excitonic and multiexcitonic fine structure [31].

Finally, we were able to interpret completely all the details of the computed optical spectrum with the help of the classification of the states. We unveiled a large number of missing transitions, which were shown to stem not only from approximate elevated symmetry, but also from approximate azimuthal and radial quantum numbers. As valence band mixing was included in the model, we could identify all the corresponding fine structure in terms of "HSBF band mixing," responsible for some spread in the optical transition spectrum, and verify analytical predictions concerning the appearance of "magic ratios" in polarization anisotropy.

High-symmetry GaAs nanowire QDs as investigated here are indeed interesting. First, since there are a large number of forbidden transitions in their optical spectrum, the multi-excitonic spectrum will also be greatly simplified and better interpreted. Second, the doubly degenerate exciton states due to symmetry are well suited for the generation of entangled photons.

ACKNOWLEDGMENTS

This work was supported by the "NANOMAT" program of Norsk Forskningsråd (Grant No. 182091). We also acknowledge support from the University Graduate Center at Kjeller, Norway. The authors would like to thank Dr. F. Michelini for a critical reading of the manuscript and useful suggestions, and Y. Sauter for useful discussions.

APPENDIX: COMPLETE D_{6h} FRAMEWORK

The following sections provide the matrix representations used for the C_{3v} and D_{6h} groups (Sec. 1), from which we deduce the HSBFs (Sec. 2). Finally, the UREF decompositions for D_{6h} are given in Sec. 3. This completes the framework needed to analyze D_{6h}.

1. Choice of standard irreducible matrix representations for C_{3v} and D_{6h}

The matrices $D^{\Gamma}(g)$ are only unique up to a similarity transform $U(\Gamma)$, i.e.,

$$D^{\Gamma^*}(g) = U(\Gamma)^{-1}\left[D^{\Gamma}_{\mathrm{Alt}}(g)\right]^{H} U(\Gamma), \tag{A1}$$

where $D^{\Gamma}_{\mathrm{Alt}}(g)$ is a matrix irrep listed in [27], and $U(\Gamma)$ is restricted to be unitary.

Note first that our matrix representation obeys transposed multiplication tables w.r.t. [27] [cf. Hermitian conjugation in Eq. (A1), this is required by our use of the passive rather than the active point of view]. Second, note on the left-hand side the presence of Γ^*, meaning the use of conjugated irreps and conjugate character table w.r.t. Refs. [12,27]. (This affects only ${}^1E_{3/2}$ and ${}^2E_{3/2}$ in C_{3v}.)

For one-dimensional irreps Γ, the set of matrices $\{D^{\Gamma}(g), g \in \mathcal{G}\}$ are simply the characters of the respective irreps, i.e., $D^{\Gamma}(g), \chi^{\Gamma} g,\ \forall\ g$, where $\chi^{\Gamma}(g)$ is listed in Ref. [27].

For two-dimensional irreps Γ, the matrices $[D^{\Gamma}_{\mathrm{Alt}}(g)]^{H}$ are not the most numerically convenient since they diagonalize rotations instead of a mirror operation w.r.t. a symmetry plane, e.g., σ_{v1} (Fig. 1). We thus choose the following to define our $D^{\Gamma}(g)$ matrices:

C_{3v}, irrep E:

$$U_{C_{3v}}(E) = \begin{bmatrix} \frac{i}{\sqrt{2}} & \frac{1}{\sqrt{2}} \\ -\frac{i}{\sqrt{2}} & \frac{1}{\sqrt{2}} \end{bmatrix}; \tag{A2}$$

C_{3v}, irrep $E_{1/2}$ (with case A in [27]):

$$U_{C_{3v}}(E_{1/2}) = \begin{bmatrix} \frac{i}{\sqrt{2}} & \frac{-1}{\sqrt{2}} \\ \frac{1}{\sqrt{2}} & \frac{-i}{\sqrt{2}} \end{bmatrix}; \tag{A3}$$

D_{6h}, irreps E_i:

$$U_{D_{6h}}(E_i) = U_{C_{3v}}(E), \quad i = 1 \ldots 2; \tag{A4}$$

D_{6h}, irreps $E_{j,k}$:

$$U_{D_{6h}}(E_{j,k}) = U_{C_{3v}}(E_{1/2}), \quad j = \frac{1}{2}, \frac{5}{2}, \quad k = u, g \tag{A5}$$

$$U_{D_{6h}}(E_{3/2,k}) = \begin{bmatrix} \frac{i}{\sqrt{2}} & \frac{1}{\sqrt{2}} \\ \frac{-1}{\sqrt{2}} & \frac{-i}{\sqrt{2}} \end{bmatrix}, \quad k = u, g. \tag{A6}$$

Note our special choice Eq. (A6) for $E_{3/2}$ in D_{6h} which stems from separate requirements concerning the "optimal" choice of HSBF: we ensured that the resulting $E_{3/2,g}$ valence band HSBF was simultaneously the same for D_{6h} and C_{3v} symmetries, so that subduction does not involve a change of basis.

2. HSBF for the conduction and valence band spinors in elevated D_{6h} symmetry

Symmetrized bases [27], also called symmetry-adapted functions (SAF), follow from subduction from $O(3)$ to D_{6h} and allow in principle to find easily the proper HSBF basis corresponding to the top (bottom) of the valence (conduction) band, respectively, of diamond or zinc blende. Unfortunately, the SAF in [27] do not have regular properties under time reversal, so some care is required.

Let us first consider the bottom of the conduction band, and use linear combinations of zone center Bloch function denoted $|\frac{1}{2}, m\rangle^{\bullet}$, $m = \pm\frac{1}{2}$, corresponding to a "quantized axis" with z along [111] and x along [11$\bar{2}$] Fig. 1. They are nearly odd under spatial inversion in GaAs (hence the $|\ldots\rangle^{\bullet}$ symbol as in [27]). Subduction from $O(3)$ tells us that the irrep $E_{1/2,u}$ of D_{6h} must be associated with this subspace. To construct the HSBF, we can either modify the SAF of [27], and use the change of basis corresponding to Eq. (A5), or equivalently decide to diagonalize the set of Wigner matrices corresponding to the symmetry operations (parametrization and factor system of [27]), and find their reduction to the set $D^{E_{1/2,u}}(g)$ given in

Appendix section 1. The resulting conduction band HSBFs are

$$\begin{aligned} |E_{1/2,u},1\rangle &= -\tfrac{1}{\sqrt{2}}\left|\tfrac{1}{2},\tfrac{1}{2}\right\rangle^{\bullet} + \tfrac{i}{\sqrt{2}}\left|\tfrac{1}{2},-\tfrac{1}{2}\right\rangle^{\bullet} \\ |E_{1/2,u},2\rangle &= \tfrac{i}{\sqrt{2}}\left|\tfrac{1}{2},\tfrac{1}{2}\right\rangle^{\bullet} - \tfrac{1}{\sqrt{2}}\left|\tfrac{1}{2},-\tfrac{1}{2}\right\rangle^{\bullet} \end{aligned}. \tag{A7}$$

For the top of the valence band, we use the set of similar Bloch functions labeled $|\frac{3}{2},m\rangle$, $m=-\frac{3}{2}\ldots\frac{3}{2}$, nearly *even* under inversion. Then, the $O(3)$ subduction tables to D_{6h} indicate reduction to the $E_{3/2,g}+E_{1/2,g}$ irreps. Again, one cannot use the SAFs of [27] if one wants to keep an invariant form of the time-reversal operator in the HSBF, therefore, we follow this time the route of reducing the Wigner matrices corresponding to symmetry operations. Using a suitable, but freely chosen, set of phase factors compatible with the irreps of Appendix section 1, one finds the following D_{6h} valence band HSBFs:

$$\begin{aligned} |E_{3/2,g},1\rangle &= -\tfrac{i}{\sqrt{2}}\left|\tfrac{3}{2},\tfrac{3}{2}\right\rangle + \tfrac{1}{\sqrt{2}}\left|\tfrac{3}{2},-\tfrac{3}{2}\right\rangle \\ |E_{3/2,g},2\rangle &= -\tfrac{1}{\sqrt{2}}\left|\tfrac{3}{2},\tfrac{3}{2}\right\rangle + \tfrac{i}{\sqrt{2}}\left|\tfrac{3}{2},-\tfrac{3}{2}\right\rangle \end{aligned} \tag{A8}$$

and

$$\begin{aligned} |E_{1/2,g},1\rangle &= \tfrac{1}{\sqrt{2}}\left|\tfrac{3}{2},\tfrac{1}{2}\right\rangle - \tfrac{i}{\sqrt{2}}\left|\tfrac{3}{2},-\tfrac{1}{2}\right\rangle \\ |E_{1/2,g},2\rangle &= -\tfrac{i}{\sqrt{2}}\left|\tfrac{3}{2},\tfrac{1}{2}\right\rangle + \tfrac{1}{\sqrt{2}}\left|\tfrac{3}{2},-\tfrac{1}{2}\right\rangle \end{aligned}. \tag{A9}$$

This choice satisfies three desirable constraints: (1) The matrix form of the time-reversal operator is invariant when the valence band basis is ordered as

$$\{|E_{3/2,g},1\rangle,|E_{1/2,g},1\rangle,|E_{1/2,g},2\rangle,|E_{3/2,g},2\rangle\}, \tag{A10}$$

hence, it preserves the canonical p,q,r,s form [Eq. (2.3)] of the Luttinger Hamiltonian in this basis. (2) It is also simultaneously a HSBF for C_{3v} (3) Their transformation laws are given by our set of standard representations listed in Appendix section 1.

For C_{3v} the choice of Eqs. (A7)–(A9) is in agreement with Ref. [23] with the correspondences

$$\begin{aligned} &|E_{1/2,u},i\rangle \to |E_{1/2},i\rangle^{\bullet}, \\ &|E_{3/2,g},i\rangle \to |^{3-i}E_{3/2}\rangle, \quad i=1\ldots2 \\ &|E_{1/2,g},i\rangle \to |E_{1/2},i\rangle, \end{aligned} \tag{A11}$$

while it differs from Ref. [12] by

$$\begin{aligned} &|E_{3/2,g},i\rangle \to (-1)^i|^iE_{3/2}\rangle \\ &|E_{1/2,g},i\rangle \to (-1)^i|E_{1/2},3-i\rangle \end{aligned}, \quad i=1\ldots2 \tag{A12}$$

where $^iE_{3/2}$ is defined with conjugated characters [cf. (A1)]. Although the two-dimensional matrix representation for $E_{1/2}$ in C_{3v} in Appendix section 1 is the same as in Ref. [12], we had chosen an opposite projective factor system for the improper operations in Ref. [12]. The present projective factor system is now the same as in [27].

3. UREF decompositions of the valence band spinors in the elevated D_{6h} symmetry

Using the HSBF derived in Appendix section 2, Eqs. (A8), (A9), and (A10), it is possible to decompose each spinor into UREFs with the help of Eq. (48) of Ref. [12] and the Clebsch-Gordon coefficients linked with the chosen standard matrix representation of Appendix section 1, and involving a minimum of arbitrary phase factors. In case of C_{3v} symmetry, one finds that the UREF decomposition of the main text [Eqs. (4.3)], which remains identical to Ref. [23] and equivalent to Ref. [12]. In case of D_{6h} symmetry, and in the HSBF basis order given by Eq. (A10), one obtains the ungerade valence band spinors given by Eq. (A13). The corresponding gerade spinors have similar expressions where $u\to g$. To lighten the notation, we have omitted the main spinor index and the HSBF index in the UREFs, but they can be retrieved easily from the main spinor and the position of the UREF [using Eq. (A10)]. For clarity, the ϕ/Φ UREFs are not the same functions in Eqs. (A13e) and (A13f) w.r.t. Eqs. (A13c) and (A13d) or Eqs. (A13a) and (A13b), and we have used the capital Φ to distinguish the E_1 and E_2 UREFs in the $E_{1/2,g}$ HSBF components from the $E_{3/2,g}$ HSBF components.

Subduction rules to C_{3v} (according to the case A in [27]) will clearly reduce the spinors (A13) to (4.3). Since E_1, $E_2\to E$ one might wonder why the partner function indices are reversed for E_1 w.r.t. E_2 (or E in C_{3v}) in Eq. (A13) [Eq. (4.3) in the main text]. The reason is simple and lies in our choice of matrix representations in Appendix section 1, where the representative of σ_{v1} has a different sign for E_1, reversing the σ_{v1} parity characteristics.

Finally, time-reversal symmetry will bring further constraints on the UREFs, e.g., via $K\underline{\psi}_1^{E_{1/2,u}}=\underline{\psi}_2^{E_{1/2,u}}$ and $K\underline{\psi}_2^{E_{1/2,u}}=-\underline{\psi}_1^{E_{1/2,u}}$ due to Kramers degeneracy. Properties similar to Eq. (4.4) can then be readily obtained, but are omitted for simplicity:

$$\underline{\psi}_1^{E_{1/2,u}} = \frac{1}{\sqrt{2}}\begin{pmatrix} \phi_1^{E_{1,u}} - \phi_2^{E_{2,u}} \\ \phi^{A_{1,u}} + \Phi_2^{E_{1,u}} \\ \phi^{A_{2,u}} + \Phi_1^{E_{1,u}} \\ \phi_2^{E_{1,u}} - \phi_1^{E_{2,u}} \end{pmatrix}, \tag{A13a}$$

$$\underline{\psi}_2^{E_{1/2,u}} = \frac{1}{\sqrt{2}}\begin{pmatrix} \phi_2^{E_{1,u}} + \phi_1^{E_{2,u}} \\ -\phi^{A_{2,u}} + \Phi_1^{E_{1,u}} \\ \phi^{A_{1,u}} - \Phi_2^{E_{1,u}} \\ -\phi_1^{E_{1,u}} - \phi_2^{E_{2,u}} \end{pmatrix}, \tag{A13b}$$

$$\underline{\psi}_1^{E_{3/2,u}} = \frac{1}{\sqrt{2}}\begin{pmatrix} \phi^{A_{1,u}} - \phi^{B_{2,u}} \\ \Phi_1^{E_{1,u}} - \Phi_2^{E_{2,u}} \\ \Phi_2^{E_{1,u}} + \Phi_1^{E_{2,u}} \\ \phi^{A_{2,u}} + \phi^{B_{1,u}} \end{pmatrix}, \tag{A13c}$$

$$\underline{\psi}_2^{E_{3/2,u}} = \frac{1}{\sqrt{2}}\begin{pmatrix} -\phi^{A_{2,u}} + \phi^{B_{1,u}} \\ \Phi_2^{E_{1,u}} - \Phi_1^{E_{2,u}} \\ -\Phi_1^{E_{1,u}} - \Phi_2^{E_{2,u}} \\ \phi^{A_{1,u}} + \phi^{B_{2,u}} \end{pmatrix}, \tag{A13d}$$

$$\underline{\psi}_1^{E_{5/2,u}} = \frac{1}{\sqrt{2}} \begin{pmatrix} \phi_2^{E_{1,u}} - \phi_1^{E_{2,u}} \\ \phi^{B_{1,u}} + \Phi_2^{E_{2,u}} \\ \phi^{B_{2,u}} + \Phi_1^{E_{2,u}} \\ \phi_1^{E_{1,u}} - \phi_2^{E_{2,u}} \end{pmatrix}, \tag{A13e}$$

$$\underline{\psi}_1^{E_{5/2,u}} = \frac{1}{\sqrt{2}} \begin{pmatrix} -\phi_1^{E_{1,u}} - \phi_2^{E_{2,u}} \\ -\phi^{B_{2,u}} + \Phi_1^{E_{2,u}} \\ \phi^{B_{1,u}} - \Phi_2^{E_{2,u}} \\ \phi_2^{E_{1,u}} + \phi_1^{E_{2,u}} \end{pmatrix}. \tag{A13f}$$

[1] L. Lauhon, M. Gudiksen, and C. Lieber, Philos. Trans. R. Soc. London **362**, 1247 (2004).
[2] A. Tribu, G. Sallen, T. Aichele, R. André, J.-P. Poizat, C. Bougerol, S. Tatarenko, and K. Kheng, Nano Lett. **8**, 4326 (2008).
[3] M. Borgström, V. Zwiller, E. Müller, and A. Imamoglu, Nano Lett. **5**, 1439 (2005).
[4] V. Kats, V. Kochereshko, A. Platonov, T. Chizhova, G. Cirlin, A. Bouravleuv, Y. Samsonenko, I. Soshnikov, E. Ubyivovk, J. Bleuse, and H. Mariette, Semicond. Sci. Technol. **27**, 015009 (2012).
[5] K. Choi, M. Arita, S. Kako, and Y. Arakawa, J. Cryst. Growth **370**, 328 (2013).
[6] S. Dorenbos, H. Sasakura, M. Van Kouwen, N. Akopian, S. Adachi, N. Namekata, M. Jo, J. Motohisa, Y. Kobayashi, K. Tomioka, T. Fukui, S. Inoue, H. Kumano, C. Natarajan, R. Hadfield, T. Zijlstra, T. Klapwijk, V. Zwiller, and I. Suemune, Appl. Phys. Lett. **97**, 171106 (2010).
[7] R. Singh and G. Bester, Phys. Rev. Lett. **103**, 063601 (2009).
[8] A. Schliwa, M. Winkelnkemper, A. Lochmann, E. Stock, and D. Bimberg, Phys. Rev. B **80**, 161307 (2009).
[9] K. F. Karlsson, M.-A. Dupertuis, D. Y. Oberli, E. Pelucchi, A. Rudra, P. O. Holtz, and E. Kapon, Phys. Rev. B **81**, 161307 (2010).
[10] D. Y. Oberli, M. Byszewski, B. Chalupar, E. Pelucchi, A. Rudra, and E. Kapon, Phys. Rev. B **80**, 165312 (2009).
[11] A. Imamoglu, D. D. Awschalom, G. Burkard, D. P. DiVincenzo, D. Loss, M. Sherwin, and A. Small, Phys. Rev. Lett. **83**, 4204 (1999).
[12] S. Dalessi and M.-A. Dupertuis, Phys. Rev. B **81**, 125106 (2010).
[13] Y.-M. Niquet and D. C Mojica, Phys. Rev. B **77**, 115316 (2008).
[14] M. Zhang and J.-J. Shi, Superlattices Microstruct. **50**, 529 (2011).
[15] V. V. Ravi Kishore, B. Partoens, and F. M. Peeters, Phys. Rev. B **82**, 235425 (2010).
[16] A. D. Andreev and E. P. O'Reilly, Appl. Phys. Lett. **79**, 521 (2001).
[17] N. Vukmirovic, D. Indjin, V. D. Jovanovic, Z. Ikonic, and P. Harrison, Phys. Rev. B **72**, 075356 (2005).
[18] S. Tomic, Phys. Rev. B **73**, 125348 (2006).
[19] C. Pryor, Phys. Rev. Lett. **80**, 3579 (1998).
[20] V. Mlinar and F. Peeters, Appl. Phys. Lett. **91**, 021910 (2007).
[21] P. Tronc, V. Smirnov, and K. Zhuravlev, Phys. Status Solidi B **241**, 2938 (2004).
[22] S. Tomic and N. Vukmirovic, J. Appl. Phys. **110**, 053710 (2011).
[23] S. Dalessi, F. Michelini, and M.-A. Dupertuis (unpublished).
[24] J. Luttinger and W. Kohn, Phys. Rev. **97**, 869 (1955).
[25] G. Fishman, Phys. Rev. B **52**, 11132 (1995).
[26] J. Guo, H. Huang, X. Ren, X. Yan, S. Cai, Y. Huang, Q. Wang, X. Zhang, and W. Wang, Chin. Opt. Lett. **9**, 041601 (2011).
[27] S. Altmann and P. Herzig, *Point-Group Theory Tables* (Clarendon, Oxford, 1994). Note: In this work we have used a passive point of view throughout. As a consequence, the group multiplication tables of Altmann should be transposed.
[28] A. Messiah, *Quantum Mechanics* (North-Holland, Amsterdam, 1959), Vol. II. Note: In this work we have used a passive point of view throughout. As a consequence, the Euler and Wigner matrices should be transposed.
[29] M. Hammermesh, *Group Theory and Its Applications to Physical Problems* (Dover, New York, 1989).
[30] B. Gallinet, J. Kupec, B. Witzigmann, and M.-A. Dupertuis, J. Opt. Soc. Am. B **27**, 1364 (2010).
[31] M.-A. Dupertuis, K. F. Karlsson, D. Y. Oberli, E. Pelucchi, A. Rudra, P. O Holtz, and E. Kapon, Phys. Rev. Lett. **107**, 127403 (2011).
[32] J. Chen, *Group Representation Theory for Physicists*, 2nd ed. (World Scientific, Singapore, 1989), Chap. 3. Note: In this paper, the class operators will be defined in the solution space, but they still enjoy all the properties derived in Chen.
[33] I. Vurgaftman, J. R. Meyer, and L. R. Ram-Mohan, J. Appl. Phys. **89**, 5815 (2001).
[34] W. Yi, V. Narayanamurti, H. Lu, M. Scarpulla, A. Gossard, Y. Huang, J.-H. Ryou, and R. Dupuis, Appl. Phys. Lett. **95**, 112102 (2009).
[35] T. Ba Hoang, A. F. Moses, L. Ahtapodov, H. Zhou, D. L. Dheeraj, A. T. J. van Helvoort, B.-O. Fimland, and H. Weman, Nano Lett. **10**, 2927 (2010).
[36] B. Gallinet, M.-A. Dupertuis, and F. Reuse (unpublished).